



Cell-Autonomous Progeroid Changes in Conditional Mouse Models for Repair Endonuclease XPG Deficiency

Sander Barnhoorn¹, Lieneke M. Uittenboogaard¹, Dick Jaarsma², Wilbert P. Vermeij¹, Maria Tresini¹, Michael Weymaere¹, Hervé Menoni¹, Renata M. C. Brandt¹, Monique C. de Waard³, Sander M. Botter⁴, Altaf H. Sarker⁵, Nicolaas G. J. Jaspers¹, Gijsbertus T. J. van der Horst¹, Priscilla K. Cooper⁵, Jan H. J. Hoeijmakers^{1*}, Ingrid van der Pluijm^{1,6*}

1 Department of Genetics, Erasmus University Medical Center, Rotterdam, The Netherlands, **2** Department of Neuroscience, Erasmus University Medical Center, Rotterdam, The Netherlands, **3** Department of Intensive Care, VU University Medical Center, Amsterdam, The Netherlands, **4** Uniklinik Balgrist, Zürich, Switzerland, **5** Life Sciences Division, Lawrence Berkeley National Laboratory, Berkeley, California, United States of America, **6** Department of Vascular Surgery, Erasmus University Medical Center, Rotterdam, The Netherlands

Abstract

As part of the Nucleotide Excision Repair (NER) process, the endonuclease XPG is involved in repair of helix-distorting DNA lesions, but the protein has also been implicated in several other DNA repair systems, complicating genotype-phenotype relationship in XPG patients. Defects in XPG can cause either the cancer-prone condition xeroderma pigmentosum (XP) alone, or XP combined with the severe neurodevelopmental disorder Cockayne Syndrome (CS), or the infantile lethal cerebro-oculo-facio-skeletal (COFS) syndrome, characterized by dramatic growth failure, progressive neurodevelopmental abnormalities and greatly reduced life expectancy. Here, we present a novel (conditional) *Xpg*^{-/-} mouse model which -in a C57BL6/FVB F1 hybrid genetic background- displays many progeroid features, including cessation of growth, loss of subcutaneous fat, kyphosis, osteoporosis, retinal photoreceptor loss, liver aging, extensive neurodegeneration, and a short lifespan of 4–5 months. We show that deletion of XPG specifically in the liver reproduces the progeroid features in the liver, yet abolishes the effect on growth or lifespan. In addition, specific XPG deletion in neurons and glia of the forebrain creates a progressive neurodegenerative phenotype that shows many characteristics of human XPG deficiency. Our findings therefore exclude that both the liver as well as the neurological phenotype are a secondary consequence of derailment in other cell types, organs or tissues (e.g. vascular abnormalities) and support a cell-autonomous origin caused by the DNA repair defect itself. In addition they allow the dissection of the complex aging process in tissue- and cell-type-specific components. Moreover, our data highlight the critical importance of genetic background in mouse aging studies, establish the *Xpg*^{-/-} mouse as a valid model for the severe form of human XPG patients and segmental accelerated aging, and strengthen the link between DNA damage and aging.

Citation: Barnhoorn S, Uittenboogaard LM, Jaarsma D, Vermeij WP, Tresini M, et al. (2014) Cell-Autonomous Progeroid Changes in Conditional Mouse Models for Repair Endonuclease XPG Deficiency. *PLoS Genet* 10(10): e1004686. doi:10.1371/journal.pgen.1004686

Editor: Laura J. Niedernhofer, The Scripps Research Institute, United States of America

Received: February 3, 2014; **Accepted:** August 19, 2014; **Published:** October 9, 2014

This is an open-access article, free of all copyright, and may be freely reproduced, distributed, transmitted, modified, built upon, or otherwise used by anyone for any lawful purpose. The work is made available under the Creative Commons CC0 public domain dedication.

Funding: We acknowledge financial support of the European commission FP7 Markage (FP7-Health-2008-200880), DNA Repair (LSHG-CT-2005-512113) and LifeSpan (LSHG-CT-2007-036894), National Institute of Health (NIH)/National Institute of Ageing (NIA) (1P01 AG-17242-02), NIEHS (1U01 ES011044), NIH/National Cancer Institute R01 CA063503 and P01 CA092584 to PKC, and the Royal Academy of Arts and Sciences of the Netherlands (academia professorship to JHJH) and a European Research Council Advanced Grant to JHJH. The research leading to these results has received funding from the European Community's Seventh Framework Programme (FP7/2007-2013) under grant agreement No. HEALTH-F2-2010-259893. The funders had no role in study design, data collection and analysis, decision to publish, or preparation of the manuscript.

Competing Interests: The authors have declared that no competing interests exist.

* Email: j.hoeijmakers@erasmusmc.nl (JHJH); i.vanderpluijm@erasmusmc.nl (IvdP)

† These authors contributed equally to this work.

Introduction

If DNA damage, either inflicted from exogenous or endogenous sources, cannot be repaired, this has detrimental consequences for an organism ranging from transcription blocks, permanent cell cycle arrest and mutations, to cell death. In the end, this unrepaired DNA damage contributes to the onset and progression of the aging process, as well as to cancer [1–3]. Cells are equipped with a set of elaborate DNA repair mechanisms integrated into a complex DNA damage response machinery that jointly attempt to fix the unrepaired DNA [4]. One such DNA repair mechanism is the Nucleotide Excision Repair (NER) pathway that removes

a wide category of helix-distorting lesions, such as those induced by UV and bulky chemical adducts, in a tightly coordinated process involving over 30 proteins [5–7]. NER can be divided into two subpathways based on the mode of damage recognition. The Global Genome (GG-)NER subpathway specifically involves the XPC and XPE protein complexes, and probes the entire genome for lesions that disrupt base-pairing [5,7–9]. Transcription-Coupled (TC-)NER, on the other hand, detects helix-distorting lesions that stall transcription in the transcribed strand of expressed genes, and hence enables resumption of transcription. TC-NER is independent of XPC and XPE and specifically involves proteins such as CSA, CSB and UVSSA [8,10,11]. After

Author Summary

Accumulation of DNA damage has been implicated in aging. Many premature aging syndromes are due to defective DNA repair systems. The endonuclease XPG is involved in repair of helix-distorting DNA lesions, and XPG defects cause the cancer-prone condition xeroderma pigmentosum (XP) alone or combined with the severe neurodevelopmental progeroid disorder Cockayne syndrome (CS). Here, we present a novel (conditional) *Xpg*^{-/-} mouse model which in a C57BL6/FVB F1 hybrid background displays many progressive progeroid features, including early cessation of growth, cachexia, kyphosis, osteoporosis, neurodegeneration, liver aging, retinal degeneration, and reduced lifespan. In a constitutive mutant with a complex phenotype it is difficult to dissect cause and consequence. We have therefore generated liver- and forebrain-specific *Xpg* mutants and demonstrate that they exhibit progressive anisokaryosis and neurodegeneration, respectively, indicating that a cell-intrinsic repair defect in neurons can account for neuronal degeneration. These findings strengthen the link between DNA damage and the complex process of aging.

lesion recognition, the subsequent ‘cut-and-patch’ core repair reaction encompasses local opening of the DNA helix and lesion verification, performed by the TFIIH complex together with XPA. Both correctly position the structure-specific endonucleases ERCC1/XPF and XPG for strand-specific excision of the lesion as part of a 22–30 bp oligonucleotide [5,7,12]. Finally, the gap is filled by repair synthesis and closed by ligation [5,7,12].

Multiple NER proteins have been attributed additional roles, both in DNA repair pathways other than NER, and in transcription regulation. For instance, TFIIH is an essential component of the general transcription machinery [13,14], but also other NER factors, including XPG and CSB, have been implicated in transcription regulation [15–18]. The 5′ endonuclease ERCC1/XPF participates in the repair of interstrand crosslinks [19,20] and subpathways of DNA double-strand break repair [21]. XPC, CSB, and XPG have been individually implicated in promoting base excision repair (BER) of oxidative DNA damage [22–30]. TFIIH and XPG are, together with CSB, thought to be involved in the early steps of Transcription-Coupled Repair (TCR), and XPG interacts directly with both CSB and RNA Polymerase II [31]. Although still controversial, there are accumulating reports that TCR not only directs NER to blocked transcription but may also recruit BER for preferential repair of oxidative DNA damage in transcribed strands [32–34]. Such a mechanism might be related to the roles of both CSB and XPG in promoting BER more globally. If correct, it could explain the much greater consequences for the organism of TCR defects compared to defects in NER alone (see below) [35].

A number of rare, autosomal recessive disorders resulting from mutations in NER genes underscore the importance of genome maintenance for the prevention of cancer as well as aging [3]. NER-associated diseases are characterized by sun (UV) hypersensitivity and include xeroderma pigmentosum (XP), UV-sensitivity syndrome (UVSS), Cockayne syndrome (CS), cerebro-oculo-facio-skeletal (COFS) syndrome, XPF-ERCC1 (XFE) progeroid syndrome, trichothiodystrophy (TTD) and disorders that combine the symptoms of these syndromes, including XP/CS [35–39]. XP originates from defects in GG-NER or total NER activity and is characterized by an over 2000-fold increased risk of cancer in sun-exposed skin and, to a much lesser extent, in internal organs [36].

XP patients may also develop progressive neurological symptoms and neuronal degeneration depending on the severity of the total NER deficiency [36,39,40]. UVSS is characterized by skin UV hypersensitivity without actually developing skin cancer. UVSS results from the selective loss of TC-NER function as a consequence of mutations in the proteins involved in detection of UV-induced transcription-blocking DNA lesions, i.e. UVSSA, CSA, and CSB [11,35,41–44]. Mutations in CSA and CSB, however, generally cause CS, a heterogeneous multisystem disorder that, in addition to UV-sensitivity, is characterized by severe growth failure and cachexia, accelerated aging features, short lifespan, and progressive sensori-neuronal abnormalities [38,45]. The severe symptoms of CS cannot be explained by the loss of TC-NER function as they do not occur in fully NER-deficient XP patients and TC-NER deficient UVSS patients. Therefore, CS symptoms have been linked to additional, yet incompletely, defined functions of CSA and CSB in DNA repair, transcription regulation, other processes, or a combination of deficiencies [3,46,47]. The same applies for mutations in the down-stream NER factors XPB, XPD, XPF, ERCC1 and XPG that cause combined XP/CS, or severe developmental/degenerative multisystem disorders such as COFS and XFE that share multiple features with severe CS forms [35,48–51]. Thus CS symptoms can result from mutations in multiple proteins that operate together in NER, but the symptoms caused by these mutations cannot be explained by NER deficiency alone, raising questions about the identities of these non-NER activities underlying CS symptoms and the extent to which different symptoms reflect deficits of different cellular processes [35,46].

Mutations in the structure-specific NER 3′-endonuclease XPG are rare, with less than 20 patients and 25 mutant alleles described so far [52–55], and cause a spectrum of disease phenotypes varying from XP to XP/CS and COFS [53]. Point mutations that selectively eliminate XPG nuclease activity cause XP, while C-terminal truncations, destabilizing point mutations, and mutations that abolish the interaction between XPG and the basal transcription factor TFIIH cause XP/CS and COFS [52–58]. These data support the notion that a deficient function of XPG outside NER is responsible for the severe CS symptoms [15,52,53,55–57].

For most NER disorders, mouse mutants have been generated that mimic the genetic defect found in patients, and to various extents reproduce XP and CS-like features as well as the progeroid hallmarks found in the corresponding human syndrome [59–62]. Accordingly, *Xpg*-null (*Xpg*^{-/-}) mice were found to develop a severe phenotype characterized by growth deficiency and very short lifespan, resembling severe XP/CS [63]. In contrast, *Xpg* mutant mice carrying amino acid substitutions that selectively abolish the nuclease function of XPG (*Xpg*^{E791A} and *Xpg*^{D811A}) show severe UV-sensitivity but normal lifespan, hence, reproducing the XP phenotype [64,65]. In addition, a mutant XPG construct containing a C-terminal truncation lacking the last 360 amino acids that was made to mimic the genotype of some XP-G/CS patients, developed a growth deficiency and short-living phenotype resembling that of *Xpg*^{-/-} mice, albeit somewhat milder [65]. Yet another C-terminal truncation mutant lacking the last 180 amino acids showed a normal lifespan, but produced a CS-like growth-deficient short-living phenotype after crossing with *Xpa*^{-/-} mice that are already fully NER-deficient [65,66]. Significantly, the same conversion of a normal lifespan into a short-living mouse model is observed after crossing CSA- or CSB-deficient CS mice with total NER- (*Xpa*^{-/-}) or GG-NER (*Xpc*^{-/-}) deficient mouse models [67–69], but not by crossing NER-deficient *Xpg*^{D811A} with *Xpa*^{-/-} mice [66]. Together these

data indicate a deleterious synergistic interaction between NER deficiency and loss of non-NER activities that underlie CS. Furthermore, they show that the C-terminus of XPG could play a role in the CS symptoms, and that the XPG-deficient *Xpg*^{-/-} mice may reproduce the phenotype of *Xpa*^{-/-}*Csb*^{-/-}, *Xpc*^{-/-}*Csb*^{-/-} or *Xpa*^{-/-}*Csa*^{-/-} double mutant mice [62,66–69].

In previous analyses we clearly observed progeroid characteristics in many NER mutant mouse models including *Xpa/Csb*, *Xpb*, *Xpd*, and *Ercc1* mutants [51,68,70–72], yet the occurrence of progeroid features in *Xpg*^{-/-} mice has hitherto been poorly established, mostly due to their very short lifespan. Since we are particularly interested in the effect of *Xpg* deletion on organ-specific aging, we generated a conditional *Xpg* mutant. As genetic background can have a significant effect on phenotype development, we first re-examined the pathological characteristics of *Xpg*^{-/-} mice in a C57BL6/FVB F1 hybrid background, as was previously described for *Ercc1* mutant mice [51,72]. In this hybrid background *Xpg*^{-/-} mice lived longer and presented progeroid features including cachexia and osteoporosis with pronounced degenerative phenotypes in both liver and brain. We next studied the effect of liver- and forebrain-specific inactivation of *Xpg*, showing that the observed phenotypes are indeed due to lack of XPG protein. Together our data show that, consistent with previous data in ERCC1- and CSB/XPA-deficient mice, *Xpg*^{-/-} mice develop a multisystem progeroid degenerative phenotype.

Results

Generation of NER-deficient *Xpg*^{-/-} mice

To generate a Cre-inducible *Xpg* knockout allele we flanked the third exon of *Xpg* with *LoxP* sites (Figure 1A). Deletion of this exon causes a frame shift and a premature translational stop immediately after exon 2 at amino acid residue 89 (instead of the full-length 1170). After transfection to 129 ES cells and selection of properly targeted clones (Figure 1B and Materials and Methods), two independent transfected clones were used to generate germline transmitting chimeras (Figure 1C). Heterozygous males, carrying the conditional *Xpg* allele, were crossed to females ubiquitously expressing *Flp* for excision of the Neomycin cassette and to yield mice that are heterozygous for the floxed *Xpg* (*Xpg*^f) allele. *Xpg*^{f/+} mice were backcrossed and maintained in FVB/N background. To generate *Xpg* mice carrying a knockout allele (*Xpg*⁻, Figure 1A), *Xpg*^{f/+} mice were crossed to *Cag-Cre* mice, which ubiquitously express Cre recombinase from germline [73], yielding heterozygous *Xpg*^{+/-} animals (Figure 1C). *Xpg*^{+/-} animals were >10 times backcrossed into C57BL6 or FVB/N genetic backgrounds. Unless otherwise stated, experiments were performed with *Xpg*^{-/-} mice in the C57BL6/FVB F1 hybrid background obtained from intercrossing C57BL6 *Xpg*^{+/-} × FVB/N *Xpg*^{+/-} animals to minimize background specific effects (see below).

The presence of a premature stop codon in the *Xpg*⁻ allele was confirmed by sequencing *Xpg* cDNA from liver of *Xpg*^{-/-} mice (Figure S1A). Accordingly, Western immunoblot analysis with an antibody raised against the central spacer region (R-domain) of XPG shows the absence of XPG protein product in mouse dermal fibroblasts (MDFs) isolated from *Xpg*^{-/-} mice (Figure 1D). Next, we tested DNA repair deficiency of *Xpg*^{-/-} MDFs. In accordance with complete NER deficiency, *Xpg*^{-/-} MDFs showed an almost 10-fold hypersensitivity to UV, similar to fully NER-defective MDFs derived from *Xpa*^{-/-} mice (Figure 1E) [74]. In addition, *Xpg*^{-/-} MDFs were hypersensitive to treatment with Illudin S (Figure 1E), consistent with the loss of TC-NER function [75], and were deficient in UV-induced unscheduled DNA synthesis in line

with loss of GG-NER activity (Figure 1F). Also, recovery of RNA synthesis after UV exposure was almost completely abolished in *Xpg*^{-/-} MDFs, further demonstrating loss of TC-NER activity (Figure 1G). *Xpg*^{-/-} MDFs showed no increased sensitivity to potassium bromate (KBrO₃) which causes oxidative DNA lesions, and a minimal increased sensitivity to the cross-linking agent cisplatin (Figure S1B).

Genetic background affects perinatal viability and lifespan of *Xpg*^{-/-} mice

In view of a significant effect of genetic background on embryonic lethality and lifespan in ERCC1-deficient mice [51,72], we examined whether a similar genetic background effect occurred in *Xpg*^{-/-} mice, by comparing birth frequencies and lifespan of *Xpg*^{-/-} mice in a C57BL6, FVB/N or a C57BL6/FVB F1 hybrid background. In C57BL6 background birth frequencies were below Mendelian expectations (~8%, Table 1), whereas in the FVB/N and C57BL6/FVB F1 hybrid background birth frequencies were Mendelian and near-Mendelian, respectively (Table 1). Also the lifespan of *Xpg*^{-/-} animals was strongly dependent on genetic background, with C57BL6 *Xpg*^{-/-} mice showing a lifespan of 3 weeks, and *Xpg*^{-/-} animals in FVB/N and C57BL6/FVB F1 hybrid background living for 15–18 weeks (Figure 2A).

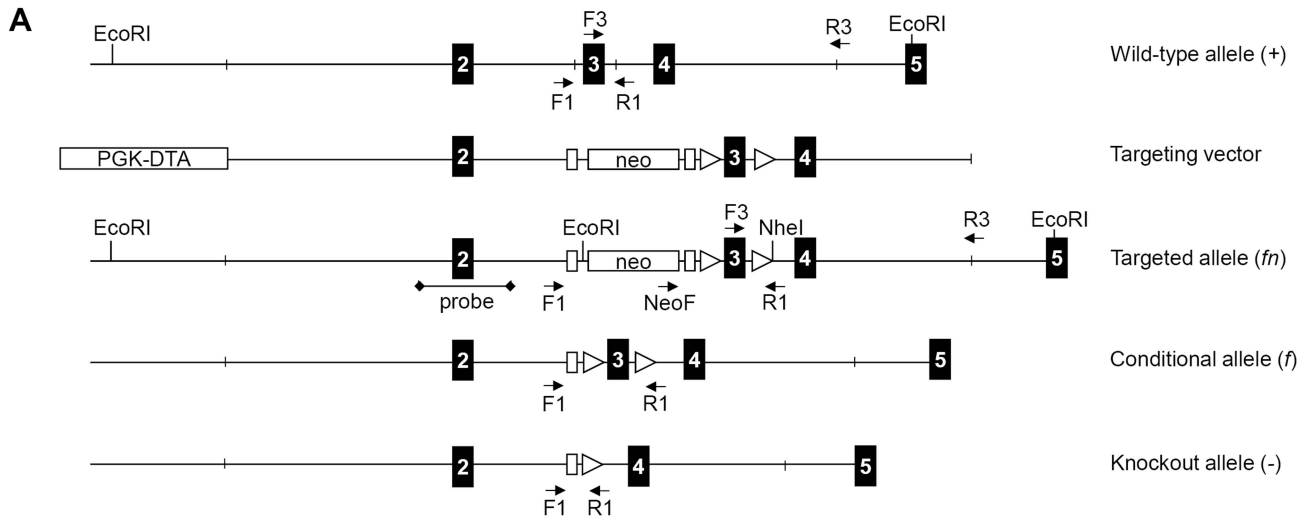
Cachexia, short lifespan and osteoporosis in *Xpg*^{-/-} mice

Further analysis of C57BL6/FVB F1 *Xpg*^{-/-} mice showed that they had the same size and weight as wild type and heterozygote littermates at late embryonic stage (E17.5; Figure 2B and C). However, after birth, *Xpg*^{-/-} mice showed reduced growth and weight gain compared to controls, and stopped growing at 6–8 weeks when their body weight was about 65–70% of that of wild type littermates (Figure 2C). From 10–11 weeks, body weights declined and the *Xpg*^{-/-} mice became progressively cachectic (Figure 2C and D). At 14 weeks all *Xpg*^{-/-} mice were severely runted (Figure 2D), and the mice died a few weeks thereafter between 15–18 weeks of age (Figure 2A and E). The growth deficiency was paralleled by the development of kyphosis (Figure 2D and F). In addition, *Xpg*^{-/-} mice progressively developed neurological symptoms, including clasping of the hind-limbs when lifted by their tails (Figure S2A), and at a later time point fine tremors (Figure 2E). Accelerating rotarod and grip strength tests in 14-week old *Xpg*^{-/-} mice revealed severe motor deficits and muscle weakness at this age (Figure S2B and C).

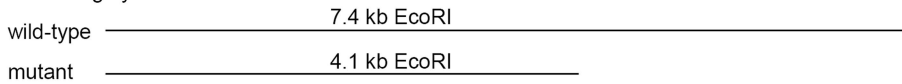
Computed tomography (CT) confirmed severe kyphosis in *Xpg*^{-/-} mice at 16 weeks of age (Figure 2F). To further examine skeletal abnormalities and the occurrence of osteoporosis as observed in other NER-deficient mouse models [68,76–79], we measured several bone parameters using femoral bones. Analysis of bone strength revealed decreased strength of the *Xpg*^{-/-} femoral bone at 14–16 weeks (Figure 2G). Micro-CT analysis showed that the thickness of the trabeculae and cortex of the femoral bones was significantly smaller in *Xpg*^{-/-} compared to wild type mice at 14–17 weeks, but not yet at 7 weeks (Figure 2H). Overall, these data indicate a progressive increase of age-related features such as osteoporosis.

Mild progeroid features and a ‘survival-like’ stress response in livers of *Xpg*^{-/-} mice

Weight loss and reduced size of *Xpg*^{-/-} mice was associated with reduced weight of internal organs (Figure S3A) and with a strong reduction in the amount of subcutaneous fat (Figure S3B). The *Xpg*^{-/-} mice previously reported by Harada et al. [63]



Screening by Southern blot:



Screening by PCR:

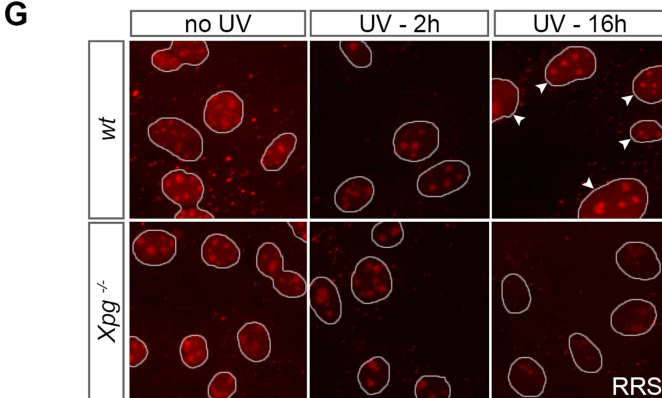
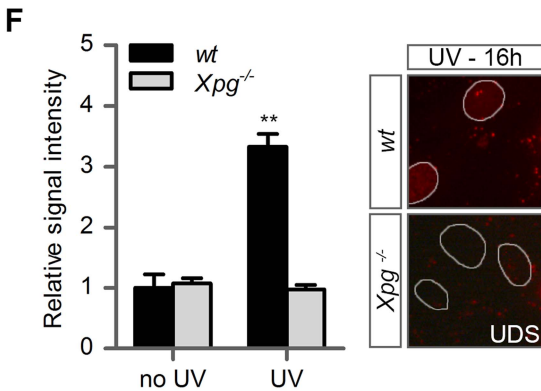
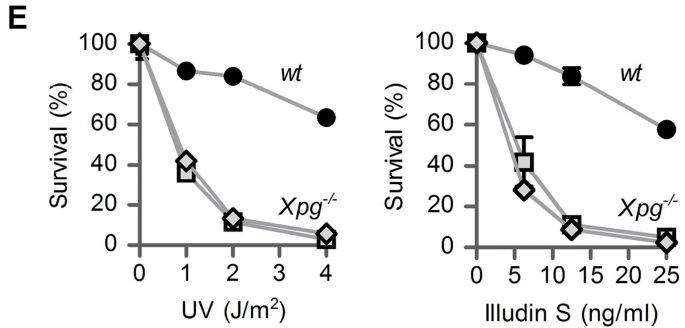
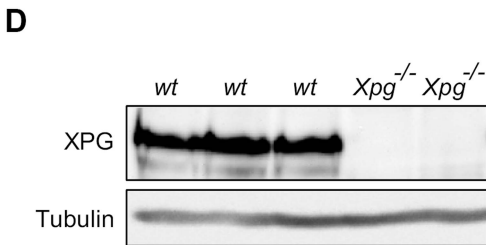
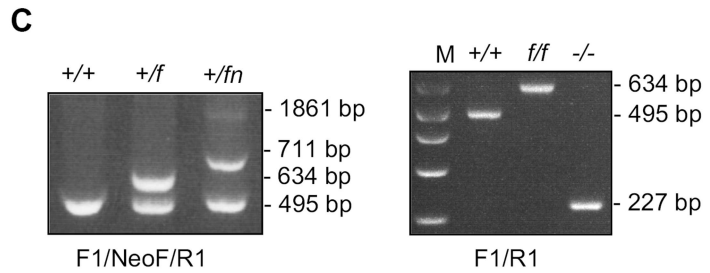
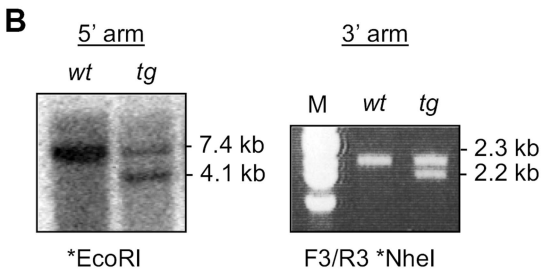
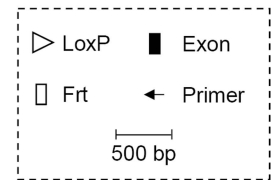
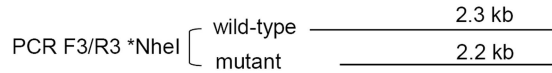


Figure 1. Generation of Xpg^{-/-} mice. (A) Genomic organization and disruption strategy for Xpg depicting the wild type allele (+), the targeting construct, the targeted allele (fn), the conditional allele after Flp-mediated recombination of Frt sites (f) and the targeted Xpg allele following subsequent Cre-mediated recombination of LoxP sites (-). Exons 2–5 are indicated by black boxes. PCR primers are shown as arrows. (B) Southern blot and PCR analysis of an ES clone showing the correct insertion of the targeting construct. ES cell genomic DNA was digested with EcoRI for Southern blot analysis and hybridized with a 0.9 kb DpnI probe. The wild type (wt) allele yields a 7.4-kb fragment whereas the targeted (tg) allele yields a 4.1-kb fragment. The NheI-digested PCR product shows the 2.3-kb and 2.2-kb bands corresponding with the wt and tg allele, respectively (see also panel A). (C) PCR detection of mouse genotypes using the primers F1, NeoF and R1 as indicated as in A. (D) Immunoblot analysis of extracts from Xpg^{-/-} and wt MDFs using a rabbit polyclonal antibody raised against a peptide conserved between human and mouse XPG. Tubulin is used as loading control. (E) Primary Xpg^{-/-} and wt MDFs, cultured at low (3%) O₂ levels were irradiated with the indicated doses of UV-C (left) or treated with the indicated doses of Illudin S for 1 h (right). After 48 h recovery, survival was assessed by cell count. (F) UV-induced UDS in primary Xpg^{-/-} and wt MDFs reveals a severe GG-NER defect in Xpg^{-/-} cells. MDFs were irradiated with 16 J/m² of UV-C. UDS levels are expressed relative to the non-irradiated wt cells. (G) UV-induced RRS in primary Xpg^{-/-} and wt MDFs reveals a severe TC-NER defect in Xpg^{-/-} cells. MDFs were irradiated with 16 J/m² of UV-C. 16 h after UV irradiation the wt cells show recovery of RNA synthesis, while Xpg^{-/-} MDFs only show residual activity in nucleoli (rRNA transcription). Arrowheads indicate nuclei. Error bars indicate standard error of the mean. **p<0.01. doi:10.1371/journal.pgen.1004686.g001

showed developmental abnormalities of the gastro-intestinal tract. These gastro-intestinal abnormalities were proposed to be a major contributor of the post-natal growth failure and short lifespan (<3 weeks) of their animals [63]. However, in contrast to their data, the gastro-intestinal tract of our Xpg^{-/-} mice had a normal size and macroscopic appearance, and showed a normal histological appearance in HE-stained sections (Figure 3A). Furthermore, staining for the proliferative cell marker Ki-67 indicated that the number of proliferative cells in the intestinal epithelium was similar between Xpg^{-/-} and wild type mice (Figure 3A). In accord with normal function of the gastro-intestinal tract we found that food intake per gram body weight was similar between wild type and Xpg^{-/-} animals (Figure S3C).

The liver is a central organ in many aspects of metabolic control, including regulation of circulating glucose levels and detoxification, and it plays a key role in regulation of IGF1-somatotrophic axis signaling. Previous studies have shown that ERCC1/XPF-deficient mice develop multiple liver abnormalities, in particular anisokaryosis resulting from polyploidy, and intranuclear inclusions [72,80–83]. Analysis of HE-stained liver sections of our Xpg^{-/-} mice revealed mild anisokaryosis, and increased mean nuclear size at 14 weeks, but not at 4 weeks of age (Figure 3B). In addition, sporadically, hepatocytes had intranuclear inclusions. These liver nuclear changes are a well characterized phenomenon in the aging liver, and indicate that Xpg^{-/-} mice show features of accelerated aging in the liver similar to Ercc1^{Δ/-} mice [72,82].

Liver cells of ERCC1-deficient and other progeroid NER-deficient mouse mutants display changes in gene expression that encompass a downregulation of catabolic and oxidative metabolism and an upregulation of antioxidant and stress defense pathways, suggestive of a compensatory survival response to cope with increased DNA damage [51,68,84,85]. To determine whether Xpg^{-/-} liver cells also display a ‘survival-like’ stress response, we determined expression levels of selected antioxidant and somatotrophic genes by real-time PCR. Indeed, mRNA levels

from a subset of antioxidant effector genes, including *Nqo1*, *Srxn1*, *Gstt2* and *Gsta1*, were significantly increased in liver homogenates of young (7-week old) Xpg^{-/-} animals compared to controls. At 14 weeks of age, we observed a similar significant increased expression of *Nqo1* and *Gsta1* while mRNA from the other antioxidant effector genes tested showed unaltered expression (Figure 3C). Expression levels of *Nrf2*, which is a potent inducer of the antioxidant response element (ARE), were unaltered, in line with the fact that NRF2-activation is largely achieved by post-translational mechanisms [86]. As increased expression of antioxidant genes could be an indication of increased genotoxic stress, we also checked the expression of the p53-responsive kinase inhibitor *p21*, a master regulator of cell survival and death [87], which is generally increased after DNA damage and was previously shown to be elevated in livers of *Ercc1* mutant mice [88]. Expression levels of *p21* doubled at the age of 7 weeks and were massively increased at the age of 14 weeks, indicative of genotoxic stress caused by the absence of XPG. To determine changes in somatotrophic gene expression we examined mRNA levels of *Ghr*, *Igf1r*, *Igf1* and *Igf1bp3*. We found a two-fold suppression of *Ghr* and *Igf1r* mRNA expression at 7 weeks, and a significant downregulation of *Ghr* mRNA levels at 14 weeks of age (Figure 3D). Together the data indicate that the Xpg^{-/-} liver in part reproduces gene expression changes observed in other short-living NER-deficient mice, which we refer to as a survival-like stress response. Finally, consistent with other NER-deficient progeroid mice [51,85], we found significantly reduced steady-state blood glucose levels in Xpg^{-/-} mice (Figure 3E).

Age-related accumulation of neurodegenerative changes in Xpg^{-/-} central nervous system

The occurrence of neurological abnormalities and impaired motor behavior in Xpg^{-/-} mice (Figure 2E and S2), as well as the abundant neurodegenerative features in ERCC1-deficient and combined XP/CS mouse models [89–91], prompted us to investigate the central nervous systems of Xpg^{-/-} animals for

Table 1. Xpg^{-/-} mice are born below Mendelian ratio in a C57BL6 background.

Total	+/+	+/-	-/-	Genetic background
60	22 (36.7%)	33 (55.0%)	5 (8.3%)**	C57BL6
39	11 (28.2%)	16 (41.0%)	12 (30.8%)	FVB/N
545	156 (28.6%)	276 (50.6%)	112 (20.6%)*	F1 (C57BL6/FVB)

Ratio of knockout mice born in different genetic backgrounds.

*p<0.05;

**p<0.01 deviation from Mendelian ratio (ChiSquaredTest).

doi:10.1371/journal.pgen.1004686.t001

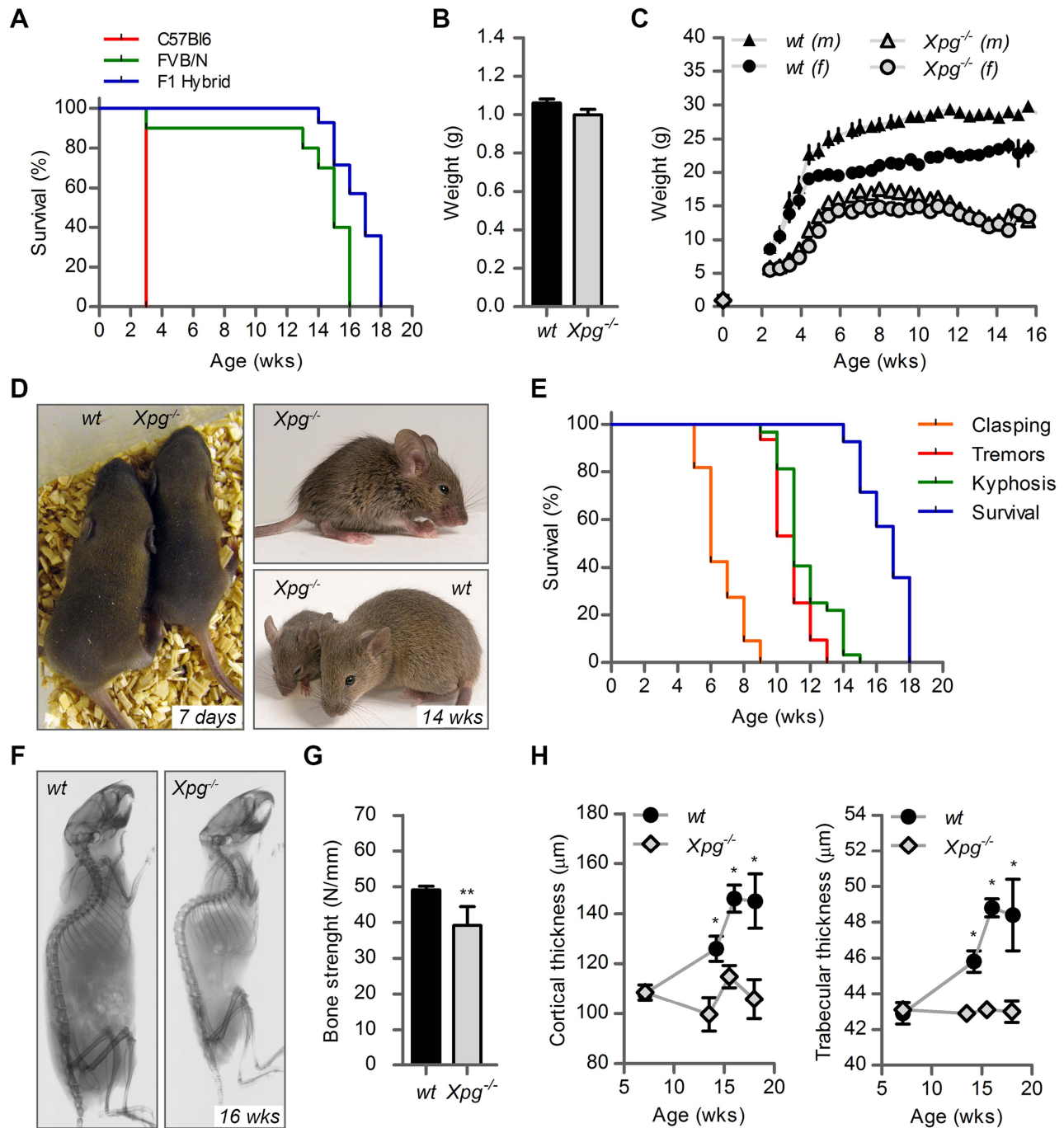


Figure 2. Progeroid characteristics of *Xpg*^{-/-} mice. (A) Survival of *Xpg*^{-/-} mice in a C57Bl6 (red), FVB/N (green) or C57Bl6/FVB F1 hybrid (blue) background; n = 5 (C57Bl6), n = 10 (FVB/N), n = 14 (C57Bl6/FVB F1 hybrid). (B) Average body weight of embryonic 17.5-day old F1 hybrid *Xpg*^{-/-} and wild type (wt) littermates; n ≥ 12 animals/group. (C) Average body weight of F1 hybrid wt males (black triangles), *Xpg*^{-/-} males (grey triangles), and *Xpg*^{-/-} females (grey circles); n ≥ 4 animals/group. (D) Left: Photograph of a 7-day old F1 hybrid *Xpg*^{-/-} and wt littermate, showing no apparent differences except a slightly smaller size. Top right: Photograph of a 14-week old *Xpg*^{-/-} mouse. Bottom right: Side by side comparison of the same 14-week old *Xpg*^{-/-} and wt littermate showing a pronounced growth deficiency of the *Xpg*^{-/-} mouse. (E) Onset of hind limb claspings (orange), tremor (red) and kyphosis (green) with age and survival of F1 hybrid *Xpg*^{-/-} mice; n = 33 (claspings, tremor and kyphosis), n = 14 (survival). (F) CT-scan of a 16-week old F1 hybrid wt (left) and *Xpg*^{-/-} (right) mouse showing prominent curvature of the spine (kyphosis) in the *Xpg*^{-/-} mouse. (G) Bone strength of F1 hybrid *Xpg*^{-/-} and wt mice analyzed by a 3-point-bending assay of the femur at an average age of 15 weeks; n ≥ 6 animals/group. (H) Cortical (left) and trabecular (right) thickness of the femora of F1 hybrid *Xpg*^{-/-} and wt mice at different ages; n = 4 animals/group. Error bars indicate standard error of the mean. *p < 0.05, **p < 0.01. doi:10.1371/journal.pgen.1004686.g002

neurodegenerative changes. Macroscopically, the brains and spinal cords of *Xpg*^{-/-} mice showed a normal appearance, albeit somewhat smaller. In addition, the gross histological organization analyzed in thionin-stained sections appeared normal in all brain regions. As a first step to examine the occurrence of neurodegenerative changes, we examined the brains of 4- and 14-week old *Xpg*^{-/-} mice immunohistologically for glial acidic filament protein (GFAP) expression, which outlines reactive astrocytosis in response to neuronal injury. A mild increase in GFAP immunostaining occurred in patches in multiple nervous system areas at 4 weeks (Figure 4A and S4A). Instead, at 14 weeks, *Xpg*^{-/-} mice showed a prominent ubiquitous increase in GFAP staining throughout the entire central nervous system including spinal cord, indicative of widespread astrocytosis (Figure 4A and S4A). Double-labelling of GFAP and the microglia cell marker Iba-1 showed that the increased GFAP staining was paralleled by microglia activation, characterized by increased Iba-1 immunoreactivity and the

transformation of resting microglia cells into activated cells with thicker processes and larger cell bodies (Figure S4B and C).

Next, to determine whether *Xpg*^{-/-} central nervous system cells experience genotoxic stress, we studied the expression of the transcription factor p53, which is activated by multiple types of DNA damage and is expressed in neurons and macroglia of many NER-deficient mouse models including mice defective in *Ercc1*, *Csa* or *Csb* [89–91]. Immunohistochemistry revealed p53-positive cells in all central nervous system regions. Analysis of the p53 density in neocortex and cerebellum indicated an increase in number of p53-positive cells in brains of 14-week old compared to 4-week old *Xpg*^{-/-} mice (Figure 4B). Similar to our findings in other NER mutant mice [89–91], double labelling of p53 with neuronal (NeuN) and astrocytic (GFAP, S100β) markers, indicated that these p53-positive cells include neurons, astrocytes (GFAP+ or S100β+; Figure S4D), and oligodendrocytes. Although not systematically investigated, we also noted that, as in other

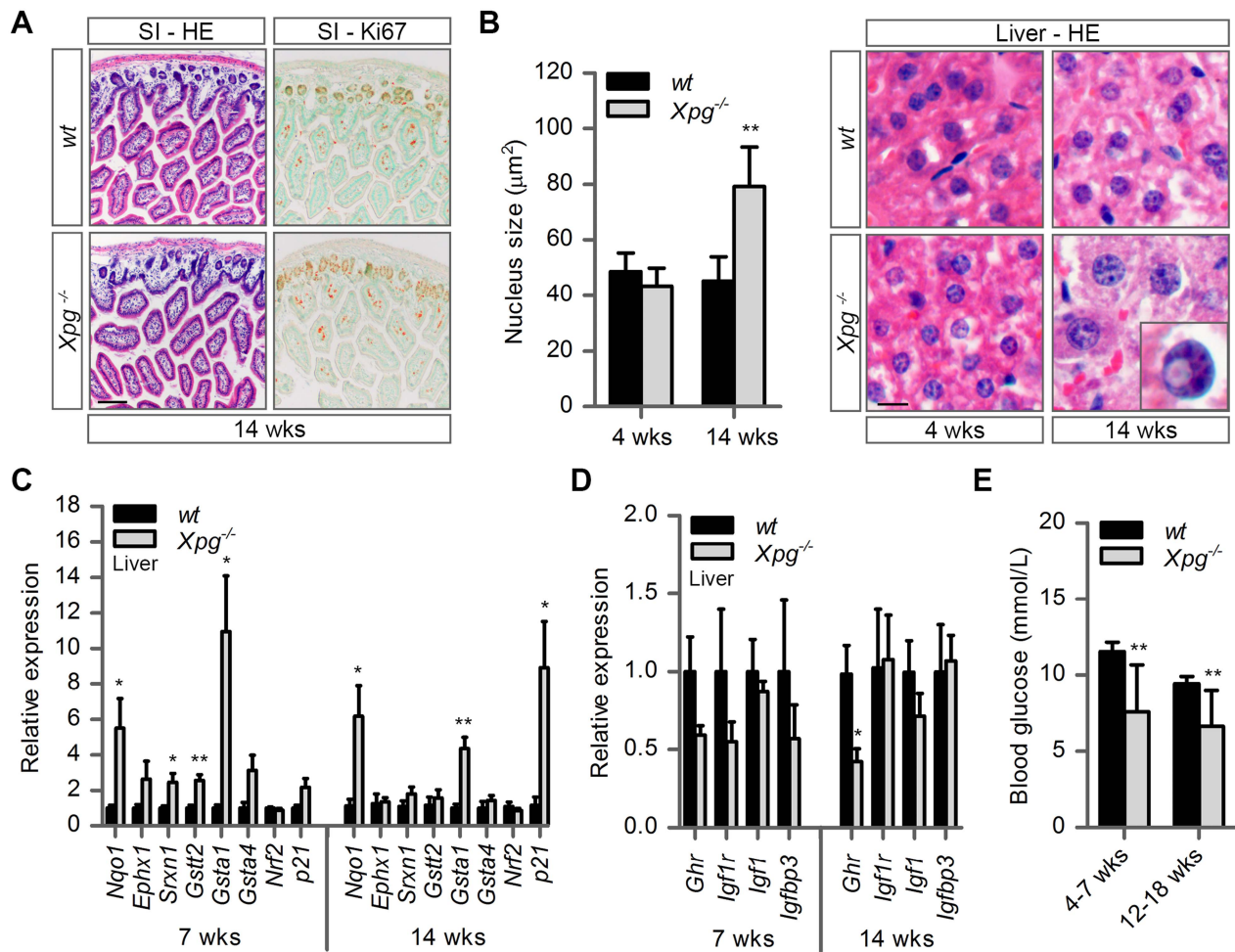


Figure 3. Intestine and liver phenotype of *Xpg*^{-/-} mice. (A) Representative images of HE and Ki67 stained small intestine (SI) of 14-week old *Xpg*^{-/-} and wild type (*wt*) mice showing no gross morphological differences. (B) Average nucleus size of hepatocytes in the liver of 4- and 14-week old *Xpg*^{-/-} and *wt* mice; n≥3 animals/group. Bottom right: magnification of a nuclear inclusion found sporadically in liver sections of 14-week old *Xpg*^{-/-} mice. (C) Relative mRNA expression levels of several antioxidant genes and the DNA damage response gene *p21* in liver tissue of 7- and 14-week old *Xpg*^{-/-} and *wt* mice. All values are corrected for *TubG2*, *Hprt*, and *Rps9* expression as internal standard and normalized to the 7-week old *wt* expression levels; n = 4 animals/group. (D) Relative expression levels of the somatotrophic genes *Ghr*, *Igf1r*, *Igf1*, and *Igf1bp3* in liver tissue of 7- and 14-week old *Xpg*^{-/-} and *wt* mice. All values are corrected for *TubG2*, *Hprt*, and *Rps9* expression and normalized to the 7-week old *wt* expression levels; n = 4 animals/group. (E) Average basal blood glucose levels in groups of 4–7 and 12–18 week old *Xpg*^{-/-} and *wt* mice; n≥15 animals/group. Scale bars: 50 μm (A), 10 μm (B). Error bars indicate standard error of the mean. *p<0.05, **p<0.01.

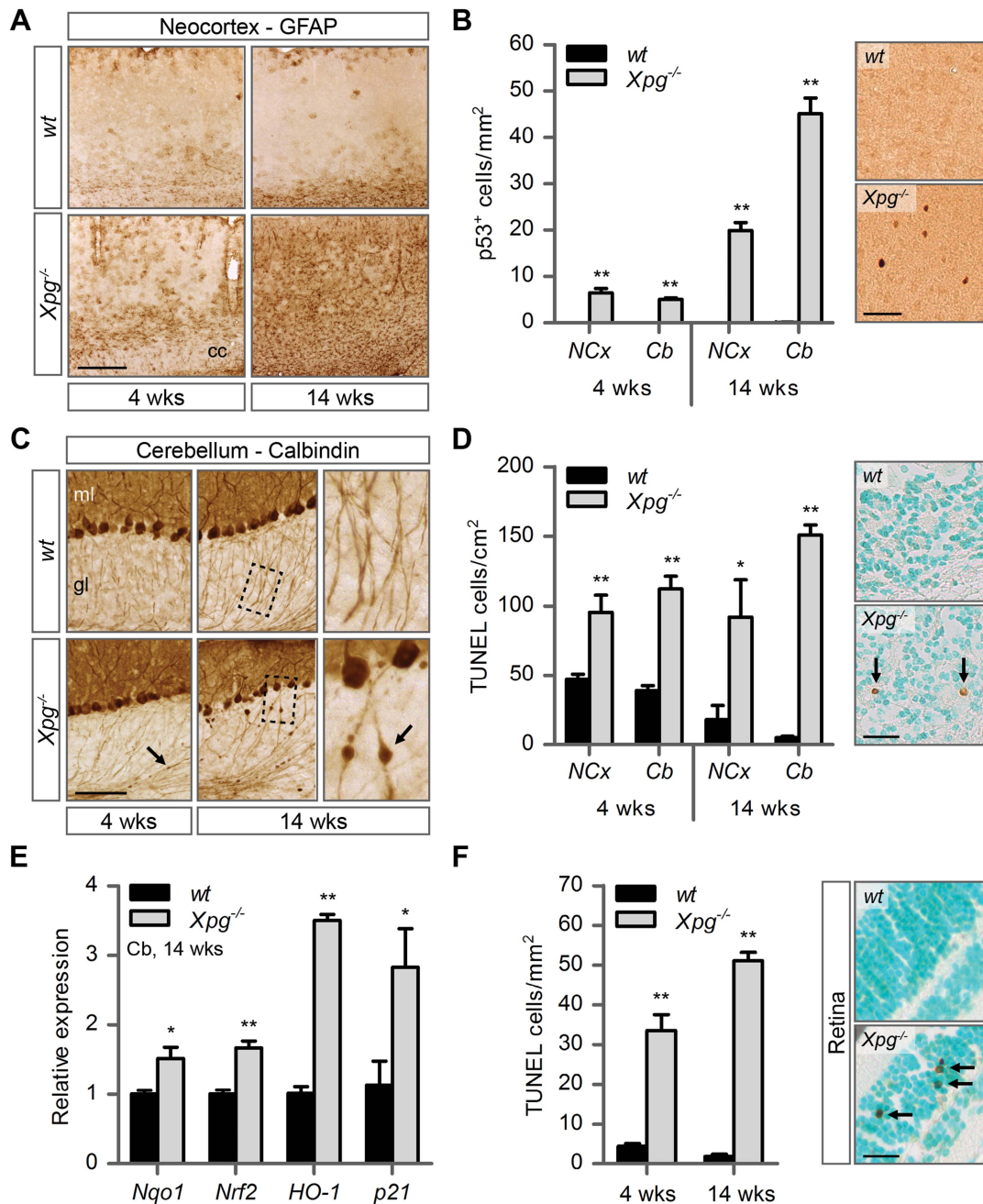


Figure 4. Increased cell death, degeneration and stress responses in post-mitotic tissues of *Xpg*^{-/-} mice. (A) Representative images of GFAP immunostained sagittal neocortex sections of 4- and 14-week old *Xpg*^{-/-} and wild type (*wt*) mice showing progressive astrocytosis in *Xpg*^{-/-} mice. cc: corpus callosum. (B) Quantification of p53-positive cells per mm² in neocortex (NCx) and cerebellum (Cb) sections of 4- and 14-week old *Xpg*^{-/-} and *wt* mice; n=3 (14 weeks) and the average of five sections of a 4-week old *Xpg*^{-/-} and *wt* animal. (C) Representative images of calbindin immunostained sagittal cerebellum sections of 4- and 14-week old *Xpg*^{-/-} and *wt* mice. Right panel: Magnification of the areas marked with dotted black boxes. Arrows indicate cerebellar torpedoes. ml: molecular layer, gl: granular layer. (D) Quantification of TUNEL-positive cells per cm² in neocortex and cerebellum sections of 4- and 14-week old *Xpg*^{-/-} and *wt* mice; n≥3 animals/group. Arrows indicate positive cells. (E) Relative mRNA expression levels of the antioxidant genes *Nqo1*, *Nrf2*, and *HO-1* and the DNA damage response gene *p21* in 14-week old *Xpg*^{-/-} and *wt* cerebellum tissue. All values are corrected for *TubG2* expression and normalized to *wt* expression levels; n=4 animals/group. (F) Quantification of TUNEL-positive cells per mm² in retinal sections of 4- and 14-week old *Xpg*^{-/-} and *wt* mice; n=6 animals/group. Arrows indicate positive cells. Scale bars: 250 μm (A), 50 μm (B), 100 μm (C), 25 μm (D, F). Error bars indicate standard error of the mean. *p<0.05, **p<0.01. doi:10.1371/journal.pgen.1004686.g004

NER-deficient mice, in neocortex and cerebellar cortex the majority of p53-positive cells were neurons, while in spinal cord a large proportion of p53-positive cells were astrocytes (Figure S4E).

To obtain evidence for the occurrence of neuronal death, we analyzed calbindin staining in cerebellar cortex where it outlines Purkinje cells and enables easy detection of the degeneration of these cells [90–92]. Calbindin staining revealed degeneration and

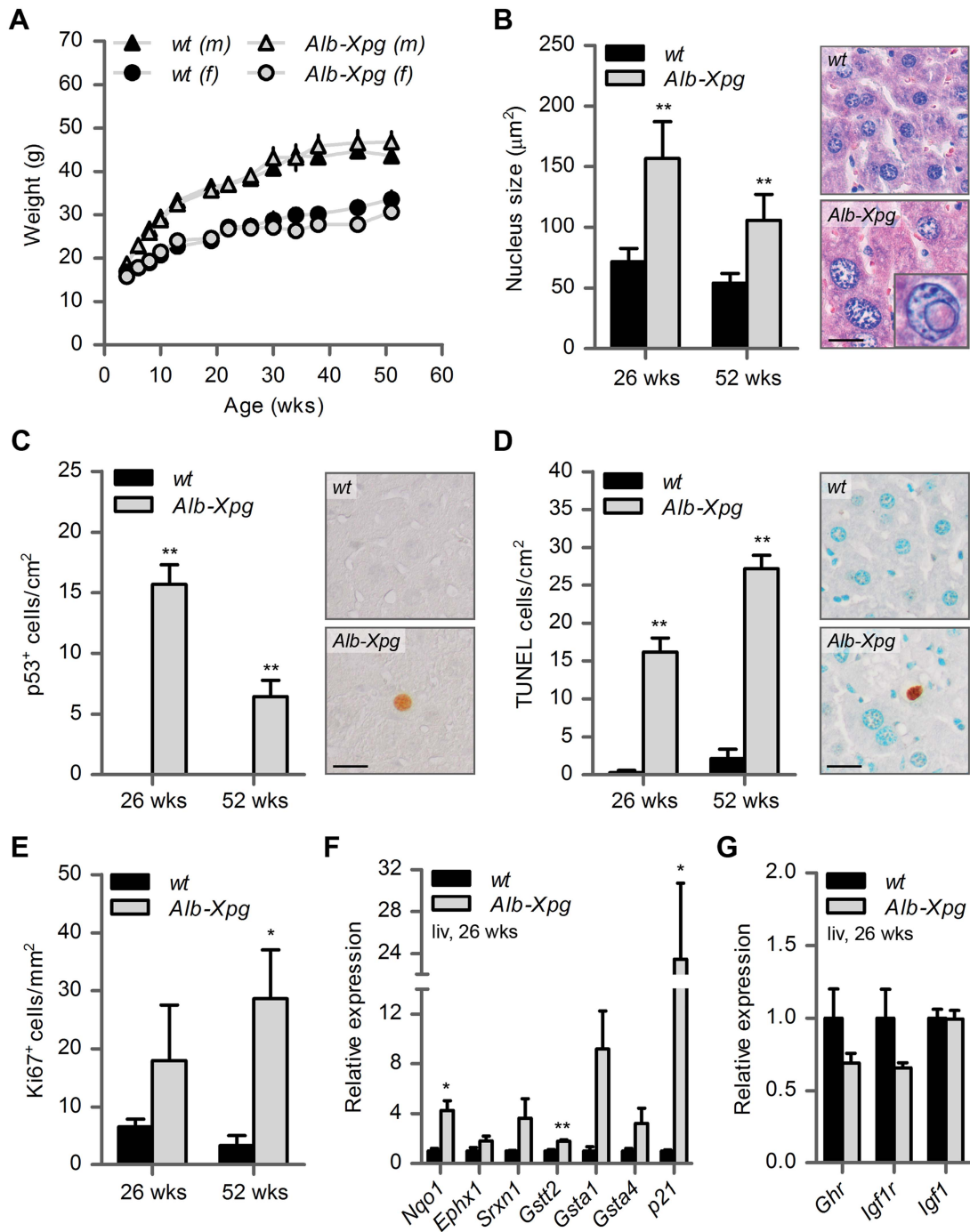


Figure 5. Aging features observed in the liver of liver-specific Xpg knockout mice. (A) Average body weight of C57Bl6/FVB F1 hybrid wild type (*wt*) males (black triangles), *wt* females (black circles), liver specific XPG-deficient (*Alb-Xpg*) males (gray triangles) and *Alb-Xpg* females (grey circles); *n* = 4 males/group, *n* = 2 females/group. (B) Average nucleus size of hepatocytes in the liver of 26- and 52-week old *Alb-Xpg* and *wt* mice; *n* = 4 animals/group. Bottom right: magnification of a nuclear inclusion found regularly in liver sections of 26- and 52-week old *Alb-Xpg* mice. (C) Quantification of p53-positive cells per cm² in the liver of 26- and 52-week old *Alb-Xpg* and *wt* mice; *n* = 3 animals/group. (D) Quantification of TUNEL-positive cells per cm² in the liver of 26- and 52-week old *Alb-Xpg* and *wt* mice; *n* = 3 animals/group. (E) Quantification of Ki67-positive cells per mm² in the liver of 26- and 52-week old *Alb-Xpg* and *wt* mice; *n* = 3 animals/group. (F) Relative mRNA expression levels of several antioxidant genes and the DNA damage response gene *p21* in liver tissue of 26-week old *Alb-Xpg* and *wt* mice. All values are corrected for *TubG2*, *Hprt*, and *Rps9* expression and normalized to *wt* expression levels; *n* = 3 animals/group. (G) Relative expression levels of the somatotrophic genes *Ghr*, *Igf1r* and *Igf1* in liver tissue of 26-week old *Alb-Xpg* and *wt* mice. All values are corrected for *TubG2*, *Hprt*, and *Rps9* expression as internal standard and normalized to *wt* expression levels; *n* = 3 animals/group. Scale bars: 25 µm (B, C, D). Error bars indicate standard error of the mean. **p* < 0.05, ***p* < 0.01. doi:10.1371/journal.pgen.1004686.g005

loss of Purkinje cells in 14-week old Xpg^{-/-} mice (Figure 4C). Also, calbindin staining revealed sporadic Purkinje cells with abnormal dendritic morphologies and, more frequently, Purkinje cells with swellings in their proximal axon (Figure 4C). Axonal swellings (also designated torpedoes or axonal spheroids) are a common feature in neurodegenerative disorders and aging [93], that is also well documented for Purkinje cell axons of CS and XP/CS patients [94]. The presence of axonal pathology indicates that many surviving Purkinje cells in 14-week old Xpg^{-/-} mice display compromised health. Notably, few small axonal swellings occurred in Purkinje cells axons in 4-week old Xpg^{-/-} mice.

To further examine the extent to which neurons in Xpg^{-/-} mice show compromised health, we examined the morphology of the Golgi apparatus in motor neurons. In a previous study in *Ercc1* mutant mice we noted that motor neurons displayed a variety of morphological abnormalities of the Golgi apparatus, and we proposed that these abnormalities reflect a heterogeneity of cellular deficits resulting from stochastic DNA damage [90]. Immunostaining for the cis-Golgi marker GM130 showed that motor neurons in Xpg^{-/-} mice developed the same heterogeneity in morphological abnormalities of the Golgi apparatus as observed in *Ercc1*^{Δ/Δ} mice. Double labelling of GM130 and p53 indicated that only a small subset of neurons with abnormal Golgi apparatus is p53 positive. This variability in p53 expression further illustrates the heterogeneity of degenerative events that may occur in Xpg^{-/-} neurons (Figure S4F).

TUNEL staining to determine the amount of apoptotic cells showed a significant increase in both the cerebrum and the cerebellum at 4 as well as 14 weeks of age (Figure 4D). Finally, real-time PCR in Xpg^{-/-} cerebellum revealed an upregulation of the p53-responsive kinase inhibitor *p21* consistent with the activation of genotoxic stress pathways (Figure 4E), and increased expression of several oxidative stress response genes (Figure 4E).

In addition to the brain and spinal cord, we also investigated the retina, as retinal degeneration is a frequent symptom of CS and XP/CS patients [38], that is also reproduced in CSA- and CSB-deficient mice [23]. TUNEL staining revealed cell death in both the inner and outer nuclear layers of the retina of 4- and 14-week old Xpg^{-/-} mice (Figure 4F). Hence, Xpg^{-/-} mice display loss of photoreceptor cells as well as degeneration of the retinal circuitry. Together these data indicate the occurrence of widespread progressive degenerative changes in Xpg^{-/-} nervous system, strongly resembling the phenotype of ERCC1-deficient mice.

Liver-specific inactivation of XPG results in progeroid features in the liver without causing early death or reduced body weight

Transgenic expression of ERCC1 in the liver has been shown to alleviate growth deficiency and to extend lifespan of ERCC1-deficient mice [83], suggesting that liver abnormalities are an important determinant of the reduced lifespan of these mice. To determine the importance of liver pathology in the runting and the reduced lifespan of our Xpg^{-/-} mice, we generated mice with liver-specific inactivation of the Xpg gene by crossing Xpg^{fl/+} mice carrying the floxed Xpg allele with heterozygous Xpg^{+/-} mice that also express the *albumin-Cre* recombinase transgene that drives Cre expression specifically in hepatocytes [95] to yield Xpg^{fl/+}/*Alb-Cre*⁺ mice, hereafter designated *Alb-Xpg* mice. This *Alb-Xpg* mouse also has the advantage that it allows to study the effect of liver XPG-deficiency in the absence of abnormalities in other tissues.

A cohort of *Alb-Xpg* mice was allowed to reach the age of one year. All *Alb-Xpg* mice displayed normal growth and weight gain, and none of them died prematurely (Figure 5A). Livers of *Alb-Xpg*

mice had an increased size compared to wild type, while brain, kidney and spleen displayed unaltered size and weight (Figure S5A). Albumin and glucose blood levels were the same as in control mice (Figure S5B and C). Histological analysis revealed anisokaryosis with karyomegaly in the liver of *Alb-Xpg* mice analyzed at 26 and 52 weeks (Figure 5B). The observed karyomegaly was more prominent than that observed in 14-week old Xpg^{-/-} mice, and cells with intranuclear inclusions were more frequent. In addition, we identified p53-positive cells, increased cell death and increased cell proliferation in *Alb-Xpg* liver consistent with a progeroid degenerative phenotype (Figure 5C–E). Furthermore, real-time PCR showed that livers of *Alb-Xpg* mice displayed a massive induction of the DNA damage response gene *p21* as well as increased expression of several antioxidant effector genes (Figure 5F). We also observed a trend of reduced expression of *Ghr* and *Igf1r* (Figure 5G), hence, reproducing gene expression changes determined in livers of Xpg^{-/-} mice. Activation of the *Nrf2* antioxidant response genes, reduction of the IGF1 axis, and increased proliferation shown by Ki67-staining are all consistent with liver regeneration after tissue damage [96]. As an additional control we showed that the expression of these genes is unaltered in livers from *Emx1-Xpg* mice that are XPG-deficient in the dorsal forebrain (see below; Figure S5D and E).

Together the data from the *Alb-Xpg* mice show that progeroid and gene expression changes in the liver triggered by the absence of XPG are not sufficient to explain the runted short-living phenotype of Xpg^{-/-} mice.

Dorsal forebrain specific inactivation of XPG results in a mixed macroglia/neuronopathy in cortex and hippocampus

Our neuropathological analyses of Xpg^{-/-} mice uncovered severe neurodegenerative changes at 14 weeks of age, compatible with neurological and motor deficits in these mice. Importantly, the presence of p53 in glia and abundant astrocytosis and microgliosis in the white matter indicate that abnormalities in Xpg^{-/-} mice are not limited to neurons, but also involve glia cells. This is consistent with our findings in CS mouse models [62,91], and with the neuropathological changes found in CS and XP/CS patients that is dominated by white matter pathology, in addition to neuronal, glial and vascular pathology, and, in severe cases, developmental abnormalities [39,94,97–99]. In previous studies, using a Cre-lox approach with *CamKIIα-Cre* and *L7-Cre* transgenic mice that drive Cre expression in post-mitotic forebrain neurons and Purkinje cells, respectively, we showed that neuron-specific deficiency of ERCC1 or combined deficiency of XPA and CSB was sufficient to trigger stochastic degeneration of these neuronal populations [89,91,92]. These studies showed that neurodegenerative changes in ubiquitous ERCC1- and XPA/CSB-deficient mice are not a consequence of developmental abnormalities, vascular problems, or degenerative changes in other organs. Furthermore, these neuron-specific mice enabled us to follow the degenerative process beyond the normal lifespan of the short-living ubiquitous ERCC1- and XPA/CSB-deficient mice [89,91,92]. In the present study we therefore used a similar approach, but with an *Emx1-Cre* transgenic line that drives Cre expression in progenitor cells of the dorsal telencephalon, to achieve inactivation of the Xpg gene not only in excitatory neurons of the neocortex and hippocampus, but also of astrocytes and oligodendrocytes in these brain areas [100]. Analysis of a cohort of *Emx1-Xpg* mice that were allowed to age for one year revealed no early death and showed that body weights were indistinguishable from that of wild type littermates until the age of 30 weeks. At older age the mean weight gain of *Emx1-Xpg* mice was

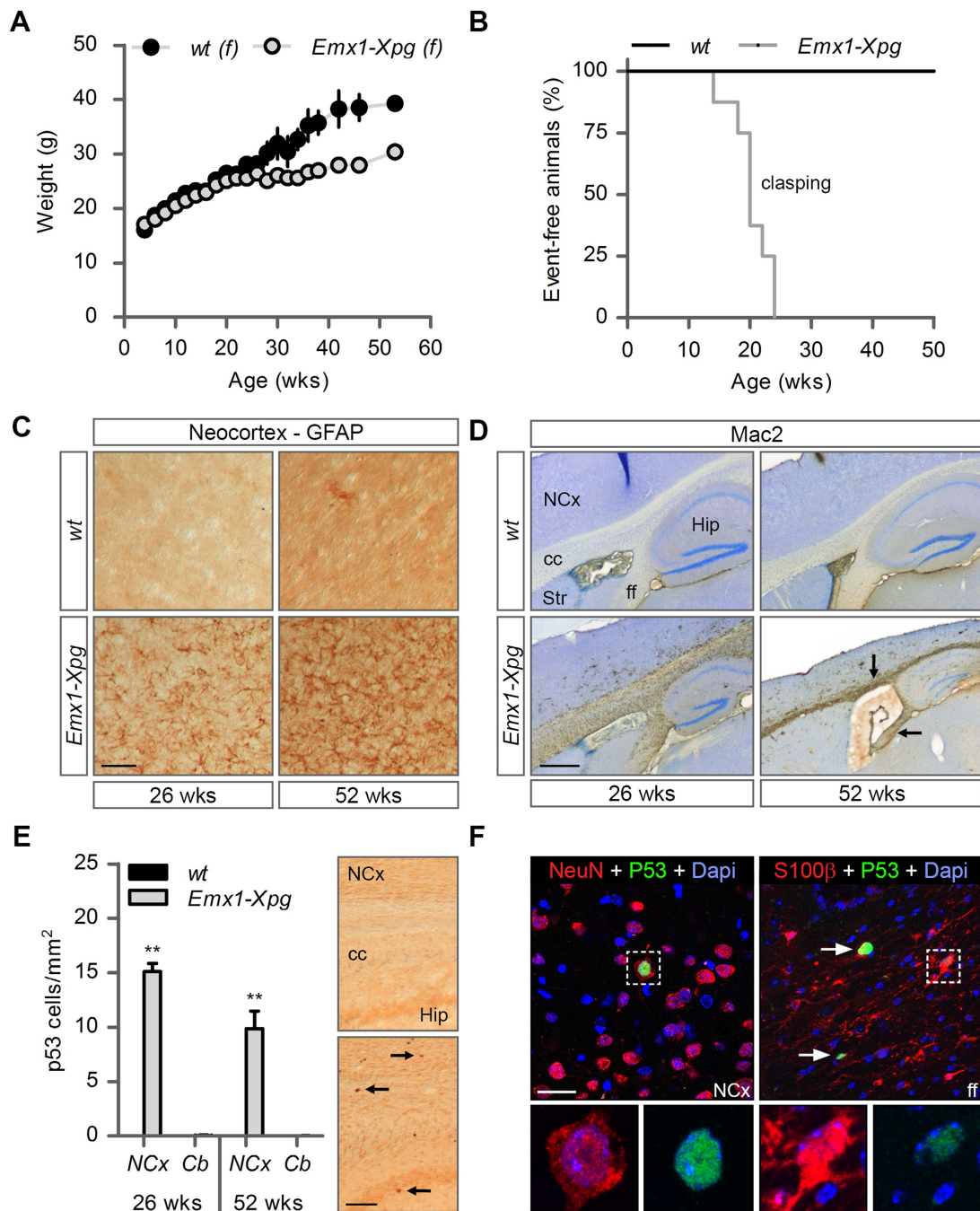


Figure 6. Age-related increase of neuronal stress in forebrain-specific *Xpg* knockout mice. (A) Average body weight of C57Bl6/FVB F1 hybrid wild type (*wt*) females (black circles) and forebrain-specific XPG-deficient (*Emx1-Xpg*) females (gray circles); $n \geq 4$ animals/group. (B) Onset of clasping of the hind limbs in *Emx1-Xpg* mice; $n = 7$ animals/group. (C) Representative images of GFAP immunostained sagittal neocortex sections of 26- and 52-week old *Emx1-Xpg* and *wt* mice showing progressive astrocytosis in *Emx1-Xpg* mice. (D) Representative images of Mac2 immunostained sagittal brain sections of 26- and 52-week old *Emx1-Xpg* and *wt* mice showing Mac2-positive microgliosis and a progressive decrease in size of the cerebral cortex and hippocampus of *Emx1-Xpg* mice. Arrows indicate microgliosis in corpus callosum and fimbria fornix. A thionin counterstaining was used. (E) Quantification of p53-positive cells in neocortex and cerebellum of 26- and 52-week old *Emx1-Xpg* and *wt* mice. Values are the average of four sections per genotype. Arrows indicate p53 positive cells. (F) Representative confocal images showing double labeled p53-NeuN cells in the neocortex (left) and p53-S100 β in the fimbria fornix (right) of 26-week old *Emx1-Xpg* mice. Arrows indicate p53 positive cells. NCx: neocortex, cc: corpus callosum, Str: striatum, ff: fimbria fornix, Hip: hippocampus. Scale bars: 50 μ m (C), 500 μ m (D), 200 μ m (E) and 20 μ m (F). Error bars indicate standard error of the mean. ** $p < 0.01$. doi:10.1371/journal.pgen.1004686.g006

significantly smaller than in control littermates (Figure 6A). This difference in weight was associated with a proportional reduced weight of internal organs (Figure S6A). Basal blood glucose concentrations were the same as in controls, indicating that reduced weight of old *Emx1-Xpg* mice is not a consequence of reduced energetic intake (Figure S6B).

To obtain a crude impression of the development of neurological symptoms, we examined the time of onset of claspings of the hind limbs when animals were lifted by their tails. This abnormality developed in *Emx1-Xpg* between 14–24 weeks of age and was not observed in control littermates (Figure 6B). The *Emx1-Xpg* mice did not develop tremors and deficits in accelerating rotarod performance (Figure S6C). Both the absence of these motor deficits and the delayed onset of claspings in comparison to the *Xpg*^{-/-} mice can be explained by the selective inactivation of *Xpg* in neocortex and hippocampus, avoiding the bulk of circuitries controlling motor behavior in mice [101].

Macroscopic inspection of brains of *Emx1-Xpg* mice at 26- and 52-week already revealed that the neocortex was considerably smaller. Histological analysis confirmed that the neocortex was thinner, and showed that also the hippocampus was dramatically smaller, while other brain regions were unaltered (Figure S6D). GFAP immunohistochemistry showed a very strong increase in GFAP staining indicative of astrogliosis in both cortex and hippocampus (Figure 6C), and no changes in other brain regions. As in the *Xpg*^{-/-} nervous system, astrogliosis was paralleled by microglial activation, identified by immunohistology with an Iba-1 antibody. Staining for Mac2 (also known as galectin-3), to outline phagocytosing microglia cells [102], revealed very high levels of Mac2-positive cells in the corpus callosum and the fimbria fornix of *Emx1-Xpg* mice (Figure 6D and S6D,E), and a moderate amount of phagocytosing microglia in the neocortex and hippocampus (Figure 6D). Remarkably, the presence of Mac2 could not be explained by axonal degeneration of cortical and hippocampal neurons solely, as we did not observe this phenomenon in our *CamKII α -Ercc1* mice [89]. Furthermore, the capsula interna of *Emx1-Xpg* mice, which contains the descending corticofugal axons and shows severe axonal degeneration, did not show this dramatic increase of Mac2 staining (Figure 6D and S6D). Hence, the presence of high levels of Mac2 labelling may reflect the same phenomenon that we observed in our CS mice, i.e. the presence of phagocytosing microglia in the absence of axonal degeneration [91]. Accordingly, we also found an upregulation of Hsp25 expression in astrocytes in the corpus callosum and fimbria fornix (Figure S6F), a phenomenon that we also observed in the white matter of CS mouse models [91]. Furthermore, analysis of p53 expression in *Emx1-Xpg* showed that multiple p53-positive cells populated the fimbria-fornix and the corpus callosum (Figure 6E). Double-labelling of p53 with NeuN or the glia marker GFAP and S100 β showed that some p53-positive cells were neurons (NeuN), but a large proportion were astrocytes (GFAP+, S100 β +), or oligodendrocytes as identified on the basis of nuclear morphology (Figure 6F). Together the data indicate that *Emx1-Xpg* mice develop a combined neuro- and gliopathy of cortex and hippocampus.

Discussion

XPG is a 3'-endonuclease that is essential for the excision step of the GG-NER and TC-NER subpathways of NER and that has additional, yet incompletely defined, roles in other repair processes and possibly in transcription [15,16,31,53,103–105]. Consistent with multiple diverse functions, mutations in XPG cause a spectrum of disease phenotypes varying from the UV-sensitivity

disorder XP to the multisystem developmental/degenerative disorders XP/CS and COFS [52–55,57]. Several *Xpg* mouse models have been generated that partially recapitulate the spectrum of genetic defects and disorders found in patients [63–66]. To better define the effect of the complete absence of XPG, in the present study we have generated mice with a Cre-inducible *Xpg* knockout allele and examined the phenotypes of total (designated *Xpg*^{-/-}), liver-specific (*Alb-Xpg*), and dorsal forebrain-specific (*Emx1-Xpg*) XPG-deficient mice. Consistent with previous data [63] we found that *Xpg*^{-/-} mice are born with normal size and weight, but progressively fail to grow and to gain weight after birth, combined with a short lifespan. In addition, we found that lifespan was influenced by genetic background, in that *Xpg*^{-/-} mice displayed a much shorter lifespan in C57BL6 background (3 weeks), compared to FVB or C57BL6/FVB F1 hybrid background (16–18 weeks). An effect of genetic background is well known for many mouse models of disease and was also noted in our *Ercc1*-mutant mice [51,72]. Differences in genetic background likely explain the differences in lifespan of our C57BL6/FVB F1 hybrid *Xpg*^{-/-} mice and the *Xpg*^{-/-} mice of Harada and coworkers [63], which all died at 3–4 weeks of age similar to our C57BL6 *Xpg*^{-/-} mice. However, what mechanism defines the short lifespan of our C57BL6 *Xpg*^{-/-} mice remains to be determined. Importantly, the effect of genetic background in mice suggests that genetic context may also impact the disease phenotype in CS and XP/CS patients. Interestingly, preliminary analysis of neuropathological changes of our C57BL6 *Xpg*^{-/-} mice at 3 weeks of age revealed subtle degenerative changes (Figure S7) that are comparable in severity to the neurodegenerative changes of C57BL6/FVB *Xpg*^{-/-} mice of 4 weeks of age, and considerably milder than those in 14-week old C57BL6/FVB F1 hybrid *Xpg*^{-/-} mice (compare Figure S7 with Figure 4). These data suggest time-dependence of the neurodegenerative phenotype and indicate that the much shorter lifespan of C57BL6 *Xpg*^{-/-} mice cannot be explained by enhanced neurodegeneration. An alternative possibility suggested by the data of Harada and coworkers [63] is that C57BL6 *Xpg*^{-/-} mice display an exaggerated developmental phenotype with more prominent developmental deficits, such as an improperly developed gastro-intestinal tract, that would reduce their ability to cope with extra-uterine life. Recent evidence from XPA/CSA-deficient mice bred in C57BL6 background suggest that providing mutant pups with soft food before weaning is sufficient to increase survival from 3–4 weeks to 12–18 weeks [106]. So far, we found no beneficial effect of soft food in our C57BL6 *Xpg*^{-/-} mice, but this remains to be further examined. Nevertheless, together the data suggest that the ability of short-living NER mutant mice to survive beyond weaning might also depend on the ability to cope with the transition from mother milk to other food.

Xpg^{-/-} mice as a progeria model

The main goal of the present study was to determine the extent to which XPG deficiency in mice results in multisystem progeroid degenerative changes as observed in CS and XP/CS patients, as well as in other NER-deficient mouse models including *Xpa/Csb*, *Xpd*, and *Ercc1* mutants [48,51,68,69,72,77,107]. Our data show that, although seemingly normal at late embryonic stage, and showing only mild degenerative features at 4 weeks of age, C57BL6/FVB *Xpg*^{-/-} at 14–16 weeks showed abundant degenerative changes in multiple tissues, indicative of accelerated aging. These degenerative/accelerated aging features included kyphosis, cachexia, osteoporosis, liver aging, and abundant nervous system degenerative changes. In addition, the data from our liver- and dorsal forebrain-specific *Xpg* mice showed that

Table 2. Comparison of the Xpg^{-/-} phenotype to that of XP/CS patients.

Phenotypic characteristics	XPG mouse	XP(G)/CS patient
UV sensitivity		
Cellular level	y	y
Organismal level	nd	y
Sensitivity to oxidative damage-cell	n	y
Growth and lifespan		
Growth retardation	y	y
Reduced subcutaneous fat	y	y
Reduced lifespan	y	y
Sensory systems		
Retinal degeneration	y	y
Sensorineuronal hearing loss	nd	y
Bones		
Osteoporosis	y	y
Kyphosis	y	y
Nervous system		
Gait ataxia	y	y
Action tremor	y	y
Cognitive decline	y	y
Brain calcifications	nd	y
Ventricle enlargement	y	y
White matter abnormalities	nd	y
Cerebral and cerebellar atrophy	y	y
Astrogliosis	y	y

y = present, n = not present, nd = not determined.
doi:10.1371/journal.pgen.1004686.t002

a much more severe tissue-specific degenerative phenotype could be obtained in these mice because of survival beyond the maximal lifespan of Xpg^{-/-} mice. Hence, the data indicate that Xpg^{-/-} mice indeed develop a multisystem premature aging phenotype reminiscent of the phenotypes of some of our other NER-deficient mouse models, in particular the *Ercc1*^{Δ/-} mice, which show a slightly longer lifespan and comparable pathological changes in liver and nervous system (see below). Moreover, the Xpg^{-/-} mouse phenotype shares many features with XP-G/CS patients [17,94,108] including a cachectic ‘frail’ appearance with loss of subcutaneous fat and signs of osteoporosis (Table 2).

Compensatory survival response in Xpg^{-/-} liver

Previously we have shown that transcription-blocking lesions trigger a “survival response” involving somatotroph attenuation and increased resistance to oxidative stress, which resembles the response triggered by dietary restriction and is associated with delaying many aspects of aging and increasing lifespan [51,68,84]. This mechanism has been observed in response to direct but persistent DNA damage as well as during the course of aging, both in natural aging as well as in specific progeroid mouse models, and is activated in long-lived mutant mice and centenarians [51,68,109]. A central hallmark of this survival response is the downregulation of genes involved in the GH/IGF axis, combined with upregulation of genes involved in the antioxidant response. Using real-time PCR for selected genes of these pathways in the present study, we show that Xpg^{-/-} mice display survival-response-like changes in gene expression in liver cells, including

a decrease in *Ghr* mRNA levels and a robust increase in expression of the antioxidant defense effector genes *Nqo1*, *Srxn1*, *Gstt2*, and *Gsta1*. Similar changes were observed in the liver of liver-specific XPG-deficient mice. Consistent with previous observations concerning the survival response, we found significantly reduced circulating glucose levels in the Xpg^{-/-} mouse. However, we found no change in glucose in the liver-specific mouse, indicating that reduced glucose levels are not necessarily a consequence of gene expression changes in the liver. We did not observe significantly lower levels of *Igf1* and *Igf1r*, as previously found for several other progeroid DNA repair mutants [51,84], although we did find a trend of reduced expression.

Increased expression of antioxidant genes was also observed in the central nervous system (i.e. cerebellum) of Xpg^{-/-} mice, but the identity and the degree of changed expression is somewhat different. For instance, *Nrf2* shows a relatively increased expression in cerebellum but not in liver, while *Nqo1* shows a very large relative increase in liver, and a modest relative increase in cerebellum. These differences may be explained by altered stress responses in different cell types [110]. In addition, in the nervous system, changes in gene expression may result from the death and disappearance of neurons and reactive proliferation of glial cells and as a consequence, reduced and increased expression of neuronal and glial genes, respectively.

Progeroid features in the livers of Xpg^{-/-} animals are not sufficient to cause reduced growth and lifespan

The liver of Xpg^{-/-} mice showed several characteristics also found in aging liver, i.e. increased nuclear size and the presence of

nuclear inclusions. These changes were much more prominent and associated with additional degenerative changes in liver-specific XPG-deficient mice. However, despite prominent liver pathology, the liver-specific Xpg^{-/-} mice at 52 weeks did not show altered weight, nor altered glucose and albumin levels suggestive of metabolic problems. Although at this point we cannot exclude that our liver-specific mutants will develop health problems in their second year of life and might develop a shorter than normal lifespan, it is safe to conclude that liver problems on their own cannot be the main culprit of the reduced lifespan and the small cachectic appearance of Xpg^{-/-} mice. In contrast to our data, findings in *Ercc1* mutant mice show that transgenic overexpression of ERCC1 in the liver alleviates growth deficiency and extends lifespan [83], indicating that liver abnormalities are an important determinant of the reduced lifespan of these mice. A possible explanation is that liver pathology is more prominent in *Ercc1* mutant mice, putatively as a consequence of additional defects in interstrand crosslink and double-strand break repair [48]. An alternative explanation for the differences in results could be that the impact of liver pathology on survival depends on the severity of pathology in other organs. This hypothesis is testable by studying survival of liver-specific ERCC1-deficient mice, and *vice versa* by generating liver-corrected Xpg^{-/-} mice using a transgenic 'rescue' strategy as reported by Selfridge et al. [83]. A possible conclusion from these studies could be that *Ercc1* and Xpg mutant mice die prematurely as a consequence of a synergistic deleterious effect of multi-organ failure. In view of the severe neurological and neurodegenerative deficits in 14–16 week old Xpg^{-/-} mice, yet an alternative scenario is that Xpg^{-/-} mice die as a consequence of nervous system abnormalities (see below). This scenario is realistic for a subset of human NER-deficient patients, in particular those developing XP with neurological abnormalities [36,40]. Interestingly, our dorsal forebrain-specific XPG-deficient mice also showed reduced weight-gain after 30 weeks of age. At this age these mice displayed severe neuronal degeneration in neocortex and hippocampus, as a result of which the mice would be expected to have severe cognitive deficits, whereas basal motor functions remain unaltered. Weight loss was not associated with altered glucose levels or gene expression changes in the liver (Figures S5 and S6). We noted the same reduced weight-gain in our forebrain neuron-specific XPA/CSB-deficient mouse model [91]. The data suggest that severe disruption of cortical or hippocampal circuitries may result in the weight loss, but the precise mechanism remains to be defined.

XPG deficiency causes age-dependent degeneration of neurons and macroglia

Our data show that Xpg^{-/-} mice, within their relatively short lifespan (16–18 weeks), develop neurological abnormalities of increasing severity in association with degenerative changes throughout the nervous system. These nervous system degenerative changes seemingly are more severe than those previously reported for another line of Xpg^{-/-} mice [111]. The differences in nervous system neurodegenerative changes can be explained by the very short lifespan (3 weeks) of previously reported Xpg^{-/-} mice, since our C57BL6 Xpg^{-/-} mice, which show the same short lifespan, also displayed a low level of nervous system pathology at the end of life (see above and Figure S7). Together with our demonstration that dorsal forebrain-specific XPG-deficient mice, allowed to age for one year, display very severe neurodegenerative changes, our data indicate that age is a key determinant in the development of neurodegenerative changes in Xpg^{-/-} mice. Our data also indicate that XPG deficiency does not result in obvious

neurodevelopmental abnormalities, although subtle developmental abnormalities cannot be excluded at this point.

The neurodegenerative changes in our Xpg^{-/-} mice strongly resemble those of incomplete ERCC1-deficient *Ercc1*^{Δ/-} mice that have a slightly longer lifespan (24–30 weeks). Our studies with *Ercc1*^{Δ/-} mice and neuron-specific *Ercc1* knock-out animals indicate that ERCC1-deficient neurons in time stochastically accumulate structural and functional deficits to eventually die and disappear [89,90,92,112]. A stochastic accumulation of deficits also appears to occur in Xpg^{-/-} neurons. Thus, the widespread distribution of astrocytosis and microgliosis, as well as p53 and TUNEL staining, indicates that degenerative changes in the Xpg^{-/-} nervous system affect all neuronal populations. The increased size and frequency of axonal spheroids in Purkinje cells, and a diversity of Golgi apparatus morphological abnormalities in motor neurons, on the other hand, illustrate that Xpg^{-/-} neurons may asynchronously accumulate a variety of degenerative features over time. This widespread and asynchronous accumulation of cellular damage in Xpg^{-/-} neurons is consistent with a model in which neurons are afflicted by stochastic DNA lesions that deregulate gene expression, as we have proposed for *Ercc1*^{Δ/-} mice [89]. A prime role for genotoxic stress in causing the degenerative phenotype in the Xpg^{-/-} nervous system is further suggested by the presence of stochastically distributed p53-positive cells and increased expression of the DNA damage responsive *p21* gene.

Together the degenerative changes in the Xpg^{-/-} nervous system favor a pathogenic model involving deficient DNA repair in the same way as proposed for ERCC1-deficient mice [48,89]. The central role of DNA damage in the Xpg^{-/-} nervous system raises questions about the identity of the DNA lesions involved. Importantly, the absence of a significant neurodegenerative phenotype in entirely NER-deficient *Xpa*^{-/-} mice has led to the conclusion that DNA lesions that accumulate in the nervous system in the absence of NER are not sufficient to trigger neuronal degeneration within the normal lifespan of mice [74,91,113]. In the case of ERCC1-deficient mice, it therefore has been proposed that the degenerative nervous system changes result from combined deficiencies in NER and other DNA repair pathways, i.e. interstrand crosslink repair and double-strand break repair [48,89]. It is possible that a similar mechanism may contribute to the severe neurodegenerative phenotype caused by XPG deficiency, as XPG has been reported to play a role in repair of crosslinks induced by mitomycin C [114]. An alternative possibility is that XPG deficiency reproduces the severe degenerative phenotype resulting from crossing NER-deficient *Xpa*^{-/-} with the *Csb*^{-/-} or *Csa*^{-/-} CS mouse models [67–69,91,106]. In this scenario XPG deficiency combines the deleterious synergistic interaction between NER deficiency and loss of the yet incompletely understood non-NER activities that underlie CS. CS proteins operate together at the interface of DNA repair and transcription regulation, and several mechanisms have been put forward to explain CS symptoms [46].

XPG can interact directly with both CSB and RNA Polymerase II [31], and may be implicated in the repair of transcription blocking oxidative lesions, for instance by recruiting base excision repair factors [32–34]. Accordingly, cells from CS patients including XP-G/CS cells have been found to display increased vulnerability to inducers of oxidative DNA lesions [55,115,116]. Importantly, Soltys et al. showed oxidative damage sensitivity of XP-G/CS, but not of XP-G patient cells [55]. Yet, in accordance with findings by Harada and coworkers [63], we found that cells from our Xpg^{-/-} mice do not display increased vulnerability to inducers of oxidative DNA lesions such as KBrO₃ (Figure S1B). This is despite clear indications of endogenous damage in, for

example, the retina of these mice, as has been previously observed for *Csb/Xpa* mice that are sensitive to oxidative damage [23]. It is currently unclear whether this is a peculiarity of these particular mouse cells in culture, as we have reported that cells from CSB-deficient mice are sensitive to IR and paraquat [117,118]. It has been argued that cultured cells may build up defense responses that mask the increased vulnerability of these cells *in vivo* [119].

To what extent do *Xpg*^{-/-} mice reproduce the nervous system abnormalities of patients carrying XPG mutations? Roughly, the progressive widespread neurodegenerative changes of *Xpg*^{-/-} mice are reminiscent of neuropathological changes of patients with ‘XP-type neurological degeneration’ [39,40,97,120]. In well documented cases these patients, carrying XPA mutations resulting in complete NER deficiency, develop a wide array of neurological symptoms that show early juvenile onset, over time become more severe, and ultimately cause premature death in mid-adult life [39,40,97]. However, the limited documented cases indicate that XP-G patients either develop no neurological symptoms, or reproduce mild to severe neurological and neuropathological features of CS [39,40,57,94,120]. In CS and XP/CS patients, neuronal degeneration generally is less prominent. Instead, these patients, including documented XP-G/CS cases, show prominent white matter degeneration, vascular pathology, calcium depositions, and, in severe cases, developmental abnormalities [39,94,97–99]. We have recently noted that CSA- and CSB-deficient CS mouse models, in addition to mild neurodegenerative changes, develop subtle white matter abnormalities and glial pathology reminiscent of the glia and white matter degenerative changes of CS patients, albeit milder [62,91]. The higher levels of neuronal degeneration in *Xpg*^{-/-} mice hamper detection of primary glial and white matter pathology, due to secondary glial pathology caused by neuronal degeneration. However, the severe white matter pathology in the corpus callosum and fimbria-fornix in our dorsal forebrain specific XPG-deficient mice strongly indicates that XPG deficiency triggers CS-like white matter pathology in mice.

Concluding remarks

In this study, we show that *Xpg*^{-/-} mice from young age onwards develop a multisystem degenerative phenotype and die before the age of 20 weeks. This phenotype strongly resembles the progeroid features of CS and XP/CS patients. In addition, the *Xpg*^{-/-} mouse model shows a number of similarities to other NER-based mouse models of progeria such as *Xpa/Csb* and *Ercc1* mutants [3,62], pointing to the importance of NER in multiple tissues. In particular, a detailed analysis of commonalities and differences between *Xpg*^{-/-} and *Ercc1* mutant mice may aid in our understanding of the contribution of different types of DNA damage and DNA repair defects in the accelerated aging process, since both endonucleases have a joint role in the damage excision step of NER but have divergent additional non-NER roles. Together our findings further stress the relationship between compromised DNA repair and acceleration of specific aging features, as well as progressive neurodegeneration. Finally, the neurodegenerative phenotype indicates that *Xpg*^{-/-} mice may serve as a model to test intervention strategies aimed at reducing the formation of detrimental DNA lesions in neurons.

Materials and Methods

Generation of a floxed *Xpg* allele

The *Xpg* targeting construct was generated using multiple elements. First, a cassette consisting of a Neomycin (NEO) resistance marker, flanked by *Frt* sites, and followed by a single

LoxP site was cloned into a modified pBlueScript SK+ vector containing a PGK-DTA negative selection marker, making use of a klenow blunted *Apal* (insert)/*XbaI*(vector) and a *NotI* restriction site. Second, *Xpg* homologous arms were PCR amplified from C57BL6 genomic DNA (originating from BAC clone RP24-343K18) and cloned into the same plasmid. The following primers (non-homologous regions indicated in italics; the *LoxP* sequence is underlined) were used for amplification of the 5' and 3' arm, respectively: LAF2 (5'-CGCACCCGGGTGTGATCCTGTGGT-CCTGTAGT-3') and LAR2 (5'-CCATCGATATCCTCAGAAAGGTATCTCTTAAGCA-3'), yielding a 3.2-kb *XmaI*-*ClaI* fragment; RAF1 (5'-CCCTGCTAGCGGATGAGGAATCGT-GACTAAGGAG-3') and RAR1 (5'-CCGACGGCGCCGCAAA-CAAGGGACCAAATGTAGCT-3'), yielding a 2.0-kb *NheI*-*NotI* fragment, where the restriction sites were introduced in the PCR primers. Last, the third exon of *Xpg* followed by a PCR-introduced *LoxP* site was amplified using the primers Ex3Lox F2 (5'-GGGAACCCGGTTTGTAGTGTCTTGTGTGACAGG-3') and Ex3LoxR2 (5'-CCCTGCTAGCATAACTTCGTATAGCA-TACATTATACGAAGTT ATCC-3'), yielding a 350-bp *AgeI*-*NheI* fragment, which was inserted between the neomycin cassette and the 5' homology arm.

Next, a total of 10 µg of *NotI*-linearized targeting vector was electroporated to *Ola129* ES cells, and the targeted clones were selected through the use of the Neomycin selection marker (G418 200 µg/ml). Clones resistant for G418 were initially screened by PCR, using a forward primer in exon 3 (F3 5'-GAGCAGGCTCTGAAAAGTCTT-3') and a reverse primer outside the 3' homologous region (R3 5'-CACTGAACAAACAAGG-GACCCAAA-3'). ES clones showing a 2.2-kb fragment in addition to the wild type 2.3-kb fragment after *NheI* digestion of the PCR product were further screened by Southern blot. ES genomic DNA was digested with *EcoRI* and hybridized with a 0.9-kb *DpnI* restriction fragment from BAC RP24-343K18, spanning the 2nd exon of *Xpg*. The probe hybridizes to a 7.4-kb fragment in wild type DNA and to an additional 4.1-kb fragment in targeted DNA.

ES cells from two independent targeted clones were micro-injected into C57BL6 blastocysts. Heterozygous mutant mice were generated by crossing the male chimeras with C57BL6 females and verified by coat color and PCR genotyping. The Neomycin (NEO) resistance gene was flanked by *Frt* sites to allow specific elimination of this dominant selectable marker by an *Flp* recombinase to avoid potential undesired influence of the *Neo* gene on *Xpg* transcription or mRNA processing. The NEO cassette was removed by crossing mice carrying the targeted allele with *Cag-Flp* recombinase FVB/N transgenic animals [121]. These mice carry the floxed allele, and are referred to as *Xpg*^{f/f} throughout this paper. Thereafter, the F₃ offspring was crossed with a *Cag-Cre* C57BL6 transgenic [73], resulting in *Cre*-mediated recombination and excision of the third exon. *Xpg*^{f/f} animals were backcrossed to C57BL6 and FVB/N in parallel, at least ten times, and interbred to obtain C57BL6, FVB/N and C57BL6/FVB F1 hybrid *Xpg*^{-/-} mice. To achieve liver specific *Xpg* gene inactivation, a transgenic line with *Cre* recombinase under the control of the albumin promoter (hereafter referred to as *Alb-Cre*) was used [95]. Female *Alb-Cre*⁺ mice were crossed with male *Xpg*^{f/f} mice (both in a C57BL6 background). Female *Xpg*^{f/f} *Alb-Cre*⁺ mice, obtained from these breedings, were crossed with male *Xpg*^{f/f} FVB/N mice to yield hybrid *Xpg*^{f/f} *Alb-Cre*⁺ mice. *Xpg*^{f/f} *Alb-Cre*⁺ mice (in a C57BL6/FVB F1 hybrid background) are heterozygous for *Xpg* in their entire body, except for the hepatocytes in the liver, which are homozygous for *Xpg* after *Cre* excision of the floxed allele. All littermates, with and without

Cre-recombinase expression were used as controls (referred to as *wt*).

FVB/N *Xpg^{fl/fl}* animals were similarly bred to the female offspring from C57BL6 *Xpg^{+/-}* and C57BL6 *Emx1-Cre* mice [100] to obtain forebrain specific XPG knock-out animals (referred to as *Emx1-Xpg*). All animals used in the studies described in this paper were of the same C57BL6/FVB F1 hybrid background (unless otherwise stated) and had *ad libitum* access to water and standard mouse food (CRM pellets, SDS BP Nutrition Ltd.; gross energy content 4.39 kcal/g dry mass, digestible energy 3.2 kcal/g or AIN93G synthetic pellets, Research Diet Services B.V.; gross energy content 4.9 kcal/g dry mass, digestible energy 3.97 kcal/g). Since the *Xpg* knockout animals were smaller, food was administered within the cages and water bottles with long nozzles were used from around two weeks of age. Experiments were performed in accordance with the Principles of Laboratory Animal Care (National Institutes of Health publication no. 86-23) and with the guidelines approved by the Erasmus University Animal Care Committee.

Genotyping

For PCR genotyping the following primers were used: F1 forward primer (5'-TCTGTTTAGGTGGTGGCCATTT-3') annealing 5' of the third exon of *Xpg*; NeoF forward primer (5'-GCTTCCTCGTGCTTTACGGTAT-3') located in the Neomycin resistance marker; R1 reverse primer (5'-CGACAGCACTTCTTTCTCCTTACT-3') annealing 3' of the third exon of *Xpg*. A 711-bp fragment was generated from the targeted allele using primers NeoF and R1, whereas a 495-bp and 227-bp fragment are amplified from the wild type and knockout allele, respectively, using the F1/R1 primerset. Cycling conditions were 95°C for 45 sec, 58°C for 45 sec, 72°C for 1 min (35 cycles), followed by an extension at 72°C for 5 min.

Sequencing

Total RNA was extracted from wild type and *Xpg^{-/-}* liver using TRIzol reagent and reverse transcribed with SuperScript II Reverse Transcriptase (Life technologies), according to the manufacturer's instructions, to generate cDNA. A 0.4-kb PCR fragment ranging from the 2nd to 6th of *Xpg* was produced using the following primers: Ex2F (5'-GCTCATCTTCTCATATATTCC-3') and Ex6R (5'-GGTAAACTCTTTCATGT-CAGTC-3') and analyzed by Sanger sequencing.

Phenotype scoring

The mice were weighed and visually inspected weekly, and were scored for the onset of various phenotypical parameters. Clasping was measured by suspending mice from their tails for 20 seconds. A clasping event was scored when retraction of both hind limbs towards the body was observed for at least 5 seconds. Whole body tremor was scored if mice were trembling for a combined total of at least 10 seconds, when put on a flat surface for 20 seconds. Mice showing an abnormal curvature of the spine were scored as having kyphosis.

Isolation and analysis of MDFs

Primary MDFs were isolated from the tail of 12–14 week old *Xpg^{-/-}* animals and wild type littermates. Minced tail skin was immersed in F10/DMEM culture medium supplemented with 20% fetal calf serum, 50 µg/ml penicillin/streptomycin, and 1.6 mg/ml type II collagenase (Gibco, Life Technologies). After incubation at 37°C for 24 hours, MDFs were filtered through

a 40 µm cell strainer, centrifuged for removal of the collagenase, and cultured at 37°C, 5% CO₂, and 3% O₂.

Immunoblot analysis of XPG protein in MDFs

Whole cell extracts were prepared from cultured MDFs using cells isolated from four wild type mice and four *Xpg^{-/-}* littermates. Proteins from 30 µl of each extract were separated by electrophoresis on 7% SDS-PAGE gels and transferred overnight onto a nitrocellulose membrane. As previously described [31], XPG protein was detected with a rabbit polyclonal antibody designated R2 (97727) that was raised against a conserved peptide from the spacer region (R-domain) of XPG corresponding to residues 267–281 of the human protein, which are identical with the same residues in mouse XPG except for amino acid 267, which is E in the human protein but Q in mouse. Whole cell extract from human embryonic kidney 293 cells was used as a positive control for XPG protein. As a loading control, tubulin was detected using a commercial antibody.

Cell survival assays

MDFs were seeded in triplicates at equal densities and treated 24 h after seeding as indicated. After 48 h recovery cell survival was determined by cell count on Beckman Coulter, Z2 Coulter particle count and size analyzer.

Unscheduled DNA Synthesis (UDS)

UDS was performed using the Click-iT EdU imaging kit (Life technologies). MDFs were seeded on coverslips and 24 h later washed with PBS and irradiated with 16 J/m² UV-C (Philips) or mock treated. Cells were directly labelled for 3 h in thymidine-free Ham's F10 medium supplemented with 10% dialyzed serum, 50 µg/ml penicillin/streptomycin, 20 µM Ethynyl-deoxyuridine and 1 µM Fluoro-desoxyuridine. After a PBS wash, the cells were chased with 10 µM non-labelled thymidine in normal medium for 15 minutes and fixed with 3.7% formaldehyde. Slides were washed 3× with PBS/3%BSA and permeabilized with PBS/0.5%Triton-X100 for 20 min. The Click-iT reaction, linking azide-conjugated Alexa dye to ethynyl groups was performed for 30 min in a dark, humid environment. After 3× PBS/3%BSA and 2× PBS wash, the slides were mounted with vectashield containing DAPI (Vector Laboratories) to stain nuclei.

Recovery of RNA Synthesis (RRS)

RRS was performed using the Click-iT EU imaging kit (Life Technologies). MDFs were seeded on coverslips and 8 h later washed with PBS and irradiated with 16 J/m² UV-C (Philips) or mock treated. After 14 h recovery, the cells were labelled for 2 h in 0.1 mM EU-containing medium (Ham's F10 medium supplemented with 10% dialyzed serum, 50 µg/ml penicillin/streptomycin and 20 mM HEPES). After a PBS wash, the cells were fixed and processed as described for UDS.

Mechanical testing of bone strength

Force-deflection curves from the left femora of 14-week-old and 16-week-old mice were acquired in a three-point bending assay using a Chatillon TCD series mechanical test frame (Technex BV, The Netherlands), equipped with 3 mm hemicylindrical supports with a 8.5 mm total span. Width between the supports was adjusted according to the anatomical landmarks of the femur, i.e. lesser trochanter and condyles. The femora were aligned such that the femoral head was in the horizontal plane and the posterior aspect of the condyles was

facing down. All samples were preconditioned for five cycles to 2 Newton (N) at a rate of 0.6 mm/min before testing to failure at a rate of 0.1 mm/min. The obtained force-deflection curves were analyzed for bone strength (N/mm), which was represented by the Δ force/deflection of the linear part of the curve.

Micro-computed tomographic (micro-CT) quantification of bone thickness

Xpg^{-/-} and wild type mice were sacrificed by cervical dislocation at scheduled ages (7, 14, 16, 18 weeks), femora were excised and non-osseous tissue was removed. Left femora were placed in PBS and stored at -20°C until further use for mechanical testing and the right femora were fixated (4% formalin). Two days post-fixation, the right femora were scanned using the Skyscan 1076 in vivo X-Ray computed tomography (Skyscan, Kontich, Belgium) with a voxel size of 8.88 μ m. Osseous tissue was distinguished from non-osseous tissue by segmenting the reconstructed grayscale images with an automated algorithm using local thresholds [122]. The region of interest (ROI), i.e. distal metaphysis of the femora, was selected by using 3D data analysis software. To compensate for bone length differences between the Xpg^{-/-} and wild type mice, the length of each ROI was determined relative to the largest specimen femur of the cohort.

Cortex and trabeculae of the metaphysis were separated using in-house developed automated software. Thickness of the trabeculae and cortices were assessed using 3D analysis software as described [123] using the CT analyzer software package (Skyscan). A bone specimen with known bone morphometrics was included within each scan as a quantitative control.

Real-time PCR

TRIzol reagent (Life Technologies) was used to isolate total RNA from mouse tissue specimens. 4 μ g RNA was reverse transcribed using SuperScript II (Life Technologies). Real-time PCR was performed on a Bio-Rad CFX96 thermocycler using SYBR Green (Sigma-Aldrich) and Platinum Taq polymerase (Life Technologies). Generation of specific PCR products was confirmed by melting-curve analysis and gel electrophoresis. For data analysis, the induction of target cDNA was calculated by the method described by [124]. p-values were determined using two-tailed t-tests. The used gene specific real-time PCR primers are listed in Supplementary Table S1.

Blood glucose and albumin levels

Mice were euthanized by CO₂ asphyxiation and blood was immediately collected from the heart. Glucose levels were measured using a Freestyle mini blood glucose meter. Albumin levels were measured in blood plasma using a mouse albumin ELISA kit (Immunology Consultants Laboratory, Inc.).

Antibodies

Primary antibodies (supplier; dilutions) used in this study were as follows: rabbit anti-Calbindin (Swant; 1:10,000); goat anti-ChAT (Millipore; 1:500); rabbit anti-GFAP (DAKO; 1:8,000); mouse anti-GM130 (BD Transduction; 1:100); rabbit anti-Hsp25 (Enzo; 1:8,000); rabbit anti-Iba-1 (Wako; 1:5,000); rat anti-Ki67 (DAKO; 1:200); rat anti-Mac2 (Cedarlane; 1:2,000); mouse anti-NeuN (Millipore; 1:1,000); rabbit anti-p53 (Leica; 1:1,000). For avidin–biotin–peroxidase immunocytochemistry biotinylated secondary antibodies from Vector Laboratories, diluted 1:200 were used. FITC-, Cy3-, and Cy5-conjugated secondary antibodies raised in donkey (Jackson ImmunoResearch) diluted at 1:200 were used for confocal immunofluorescence.

Histological procedures

TUNEL staining on liver, brain and retina: To quantify apoptotic cells, specimens were fixed overnight in 10% buffered formalin, paraffin-embedded, sectioned at 5 μ m, and mounted on Superfrost Plus slides. Paraffin sections were employed for TdT-mediated dUTP Nick-End Labeling (TUNEL) assay using a commercial kit (Apoptag Plus Peroxidase in situ apoptosis detection kit, Millipore). Sections were deparaffinized and incubated as described by the manufacturer. HE staining on liver, skin and small intestine: Liver, skin and intestine specimens were processed using the same fixation and sectioning methods as described for the TUNEL staining. Paraffin sections were deparaffinized, rehydrated in decreasing concentrations of ethanol and stained with haematoxylin and eosin.

For immunohistochemistry, paraffin sections of liver and intestine specimens were deparaffinized, rehydrated in decreasing concentrations of ethanol, treated for 10 minutes with 3% H₂O₂ to quench endogenous peroxidase activity and heated to 100°C for 1 h in 10 mM sodium citrate buffer, pH 6, for antigen retrieval. The amount of damaged (p53) and proliferating (Ki67) cells were subsequently detected using the avidin–biotin–immunoperoxidase complex method (ABC, Vector Laboratories, USA) with diaminobenzidine (0.05%) as chromogen.

Gelatin sections of brain and spinal cord: Mice were anaesthetized with pentobarbital and perfused transcardially with 4% paraformaldehyde. Brain and spinal cord were dissected out, post-fixed for 1 h in 4% paraformaldehyde, cryoprotected, embedded in 12% gelatin, rapidly frozen, and sectioned at 40 μ m using a freezing microtome or stored at -80°C until use. Frozen sections were processed free floating using the ABC method (ABC, Vector Laboratories, USA) or single-, double-, and triple-labelling immunofluorescence. Immunoperoxidase-stained sections were analyzed and photographed using an Olympus BX40 microscope. Immunofluorescence sections were analyzed using a Zeiss LSM700 confocal.

Rotarod performance

Average time spent on an accelerating rotarod (Ugo Basile). Xpg^{-/-} mice and wild type controls were given four consecutive trials of maximally 5 minutes with inter-trial intervals of 1 hour. Emx1-Xpg mice were given two trials per day with a 1 hour inter-trial interval for four consecutive days.

Grip strength

Grip strength was determined by placing mice with forelimbs or all limbs on a grid attached to a force gauge, and steadily pulling the mice by their tail. Grip strength is defined as the maximum strength produced by the mouse before releasing the grid. For each value the test is performed in triplicate.

Statement of ethical approval

This study was performed in strict accordance with the recommendations in the Guide for the Care and Use of Laboratory Animals of the National Institutes of Health. The protocol was approved by the Committee on the Ethics of Animal Experiments of the Erasmus MC (Permit Numbers: 139-03-08, 139-09-03, 139-12-18).

Supporting Information

Figure S1 (A) Recombination of *Frt* and *LoxP* sites yield a Xpg^{-/-} genetic status with a premature STOP codon in exon 3 as shown by Sanger sequencing of mRNA isolated from Xpg^{-/-} liver tissue. (B) Primary Xpg^{-/-} and wild type (*wt*) MDFs, cultured at low (3%)

O₂ levels were treated with the indicated doses of KBrO₃ (left) or cisplatin (right) for 1 h. After 48 h recovery, survival was assessed by cell count. Error bars indicate standard error of the mean. (TIF)

Figure S2 (A) Tail suspension test of 16-week old Xpg^{-/-} and wild type (*wt*) mice showing normal spreading of the hind limbs in *wt* mice, while Xpg^{-/-} mice display clasping. (B) Rotarod performance of 14-week old Xpg^{-/-} and *wt* mice. Trials were performed with 1 h intervals; n = 4 animals/group. (C) Average grip strength of the forelimbs and all limbs of 14-week old Xpg^{-/-} and *wt* mice; n = 4 animals/group. Error bars indicate standard error of the mean. **p < 0.01. (TIF)

Figure S3 (A) Absolute weight of liver, brain, kidney and spleen from 4- and 14-week old Xpg^{-/-} and wild type (*wt*) males: n = 3 (4 weeks), n = 18 (14 weeks). (B) Representative images of HE stained skin patches of 4-week old Xpg^{-/-} and *wt* mice. Dotted arrows indicate dermis (d) thickness, which is similar between *wt* and Xpg^{-/-} mice, while subcutaneous fat (sf) is severely reduced in Xpg^{-/-} mice as indicated with solid arrows. (C) Relative food intake of Xpg^{-/-} males (grey triangles), Xpg^{-/-} females (grey circles), *wt* males (black triangles) and *wt* females (black circles); n = 6 animals/group. Scale bars: 50 μm (B). Error bars indicate standard error of the mean. *p < 0.05, **p < 0.01. (TIF)

Figure S4 (A) Representative images of GFAP immunostained sagittal brain sections of 4- and 14-week old Xpg^{-/-} and wild type (*wt*) mice showing progressive astrocytosis in Xpg^{-/-} mice. Magnifications of the areas marked with black dotted squares are shown in figure 4A. (B) Confocal images showing a double labeling of Iba1-GFAP in the neocortex of 4- and 14-week old Xpg^{-/-} and *wt* mice. Right panels are magnifications of the areas marked with the white dotted boxes. Arrowheads indicate resting microglia, while arrows indicate active microglia frequently found in 14-week old Xpg^{-/-} mice. (C) Confocal images showing a double labeling of Iba1-GFAP in the spinal cord of 14-week old Xpg^{-/-} and *wt* mice. Right panels are magnifications of the areas marked with the white dotted boxes. Arrowheads indicate resting microglia, while arrows indicate active microglia frequently found in Xpg^{-/-} mice. (D) Confocal images of double labeled p53-NeuN and p53-S100β cells in the neocortex of 14-week old Xpg^{-/-} mice showing p53 staining in both neurons and astrocytes. (E) Confocal images of double labeled p53-NeuN cells in the spinal cord of 14-week old Xpg^{-/-} mice showing p53 staining mostly in non-neuronal cells. Right panels are magnifications of the areas marked with white dotted boxes. Arrowheads indicate non-neuronal p53 positive cells, while the white arrow indicates a p53 positive neuronal cell. The double arrow points to a p53 positive motor neuron. (F) Confocal images showing a triple immunostaining of GM130, p53 and ChAT in the spinal cord of 14-week old Xpg^{-/-} mice. Abnormal cis-Golgi in ChAT positive motor neurons can be found in both p53 positive and negative cells. The yellow arrow indicates a p53 positive motor neuron with abnormal cis-Golgi, while the blue arrow points to a p53 negative motor neuron. Scale bars: 1000 μm (A), 200 μm (B, C, E), 20 μm (D, F). (TIF)

Figure S5 (A) Absolute weight of liver, brain, kidney and spleen from 26- and 52-week old *Alb-Xpg* and wild type (*wt*) males: n = 3 (26 weeks), n = 5 (52 weeks). (B) Albumin concentration in plasma of 26- and 52-week old *Alb-Xpg* and *wt* mice; n ≥ 2 animals/group. (C) Average basal blood glucose levels of 26- and 52-week old *Alb-*

Xpg and *wt* mice; n = 3 (26 weeks), n = 5 (52 weeks). (D) Relative mRNA expression levels of several antioxidant genes and the DNA damage response gene *p21* in 26-week old *Emx1-Xpg* liver. All values are corrected for *TubG2*, *Hprt*, and *Rps9* (Table S1) expression and normalized to *wt* expression levels; n = 3 animals/group. (E) Relative expression levels of the somatotropic genes *Ghr*, *Igf1r* and *Igf1* in liver tissue of 26-week old *Emx1-Xpg* mice. All values are corrected for *TubG2*, *Hprt*, and *Rps9* and normalized to the 26-week *wt* expression levels; n = 3 animals/group. Error bars indicate standard error of the mean. *p < 0.05. (TIF)

Figure S6 (A) Absolute weight of liver, brain, kidney and spleen from 26- and 52-week old *Emx1-Xpg* and wild type (*wt*) females: n = 3 (26 weeks), n = 6 (52 weeks). (B) Average basal blood glucose levels of 26- and 52-week old *Emx1-Xpg* and *wt* mice; n = 3 (26 weeks), n = 6 (52 weeks). (C) Rotarod performance of 26-week old *Emx1-Xpg* and *wt* mice. Average of two trials given for four consecutive days; n = 5 animals/group. (D) Representative images of Mac2 immunostained sagittal brain sections of 26- and 52-week old *Emx1-Xpg* and *wt* mice showing Mac2-positive microgliosis and a progressive decrease in size of the cerebral cortex and hippocampus of *Emx1-Xpg* mice. A thionin counterstaining was used. (E) Magnification of the marked areas indicated in S6D. (F) Representative images of Hsp25 immunostained sagittal brain sections of 26- and 52-week old *Emx1-Xpg* and *wt* mice showing high levels of Hsp25 in the corpus callosum and fimbria fornix of *Emx1-Xpg* mice (arrows), but not in the descending corticofugal axons of the capsula interna which run through the striatum (arrowhead). NCx: neocortex, Str: striatum, Hip: hippocampus, Th: thalamus, Mes: mesencephalon, MeO: medulla oblongata, Cb: cerebellum, cc: corpus callosum, ff: fimbria fornix. Scale bars: 1000 μm (D), 50 μm (E), 500 μm (F). Error bars indicate standard error of the mean. *p < 0.05, **p < 0.01. (TIF)

Figure S7 (A) Representative images of GFAP immunostained neocortex sections of 3-week old C67Bl6 Xpg^{-/-} and *wt* mice showing mild astrocytosis in the Xpg^{-/-} mice. cc: corpus callosum. (B) Representative images of calbindin immunostained cerebellum sections of 3-week old C67Bl6 Xpg^{-/-} and *wt* mice showing subtle neuropathology in the Xpg^{-/-} mice. ml: molecular layer, gl: granular layer. (C) Quantification of p53-positive cells per mm² in neocortex (NCx) and cerebellum (Cb) of 3-week old C67Bl6 Xpg^{-/-} and *wt* mice. Values are the average of three sections per genotype. Scale bars: 250 μm (A), 100 μm (B, C). Error bars indicate standard error of the mean. **p < 0.01. (TIF)

Table S1 Primer sequences for real-time PCR. (DOCX)

Acknowledgments

We would like to thank Nils Wijgers for providing the UDS and RRS protocol & reagents and Yanto Ridwan and Sylvia Gabriels for general assistance with mouse experiments. We would also like to thank Ruud Koppelman for taking photographs of the Xpg^{-/-} mouse.

Author Contributions

Conceived and designed the experiments: SB LMU DJ WPV MCdW SMB JHJH IvdP. Performed the experiments: SB LMU DJ WPV MT MW HM RMCB SMB AHS. Analyzed the data: SB LMU DJ WPV SMB. Wrote the paper: SB LMU DJ WPV NGJJ GTJvdH PKC JHJH IvdP.

References

- Hanahan D, Weinberg RA (2011) Hallmarks of cancer: the next generation. *Cell* 144: 646–674.
- Lopez-Otin C, Blasco MA, Partridge L, Serrano M, Kroemer G (2013) The hallmarks of aging. *Cell* 153: 1194–1217.
- Hoeijmakers JH (2009) DNA damage, aging, and cancer. *N Engl J Med* 361: 1475–1485.
- Hoeijmakers JH (2001) Genome maintenance mechanisms for preventing cancer. *Nature* 411: 366–374.
- Fagbemi AF, Orelli B, Scharer OD (2011) Regulation of endonuclease activity in human nucleotide excision repair. *DNA Repair (Amst)* 10: 722–729.
- Friedberg EC, Aguilera A, Gellert M, Hanawalt PC, Hays JB, et al. (2006) DNA repair: from molecular mechanism to human disease. *DNA Repair (Amst)* 5: 986–996.
- Scharer OD (2013) Nucleotide excision repair in eukaryotes. *Cold Spring Harb Perspect Biol* 5: a012609.
- Hanawalt PC (2008) Emerging links between premature ageing and defective DNA repair. *Mech Ageing Dev* 129: 503–505.
- Naegeli H, Sugawara K (2011) The xeroderma pigmentosum pathway: decision tree analysis of DNA quality. *DNA Repair (Amst)* 10: 673–683.
- Fousteri M, Mullenders LH (2008) Transcription-coupled nucleotide excision repair in mammalian cells: molecular mechanisms and biological effects. *Cell Res* 18: 73–84.
- Vermeulen W, Fousteri M (2013) Mammalian transcription-coupled excision repair. *Cold Spring Harb Perspect Biol* 5: a012625.
- Staresinic L, Fagbemi AF, Enzlin JH, Gourdin AM, Wijgers N, et al. (2009) Coordination of dual incision and repair synthesis in human nucleotide excision repair. *EMBO J* 28: 1111–1120.
- Egly JM, Coin F (2011) A history of TFIIH: two decades of molecular biology on a pivotal transcription/repair factor. *DNA Repair (Amst)* 10: 714–721.
- Giglia-Mari G, Coin F, Ranish JA, Hoogstraten D, Theil A, et al. (2004) A new, tenth subunit of TFIIH is responsible for the DNA repair syndrome trichothiodystrophy group A. *Nat Genet* 36: 714–719.
- Ito S, Kuraoka I, Chymkowitz P, Compe E, Takedachi A, et al. (2007) XPG stabilizes TFIIH, allowing transactivation of nuclear receptors: implications for Cockayne syndrome in XP-G/CS patients. *Mol Cell* 26: 231–243.
- Le May N, Fradin D, Iltis I, Bougneres P, Egly JM (2012) XPG and XPF Endonucleases Trigger Chromatin Looping and DNA Demethylation for Accurate Expression of Activated Genes. *Mol Cell* 47: 622–632.
- Scharer OD (2008) XPG: its products and biological roles. *Adv Exp Med Biol* 637: 83–92.
- Lake RJ, Fan HY (2013) Structure, function and regulation of CSB: a multi-talented gymnast. *Mech Ageing Dev* 134: 202–211.
- Su Y, Orelli B, Madiredy A, Niedernhofer LJ, Scharer OD (2012) Multiple DNA binding domains mediate the function of the ERCC1-XPF protein in nucleotide excision repair. *J Biol Chem* 287: 21846–21855.
- Klein Douwel D, Boonen RA, Long DT, Szypowska AA, Raschle M, et al. (2014) XPF-ERCC1 Acts in Unhooking DNA Interstrand Crosslinks in Cooperation with FANCD2 and FANCP/SLX4. *Mol Cell* 54: 460–471.
- Ahmad A, Robinson AR, Duensing A, van Drunen E, Beverloo HB, et al. (2008) ERCC1-XPF endonuclease facilitates DNA double-strand break repair. *Mol Cell Biol* 28: 5082–5092.
- D'Errico M, Parlanti E, Teson M, de Jesus BM, Degan P, et al. (2006) New functions of XPC in the protection of human skin cells from oxidative damage. *EMBO J* 25: 4305–4315.
- Gorgels TG, van der Pluijm I, Brandt RM, Garinis GA, van Steeg H, et al. (2007) Retinal degeneration and ionizing radiation hypersensitivity in a mouse model for Cockayne syndrome. *Mol Cell Biol* 27: 1433–1441.
- Melis JP, Luitjen M, Mullenders LH, van Steeg H (2011) The role of XPC: implications in cancer and oxidative DNA damage. *Mutat Res* 728: 107–117.
- Trapp C, Reite K, Klungland A, Epe B (2007) Deficiency of the Cockayne syndrome B (CSB) gene aggravates the genomic instability caused by endogenous oxidative DNA base damage in mice. *Oncogene* 26: 4044–4048.
- Menoni H, Hoeijmakers JH, Vermeulen W (2012) Nucleotide excision repair-initiating proteins bind to oxidative DNA lesions in vivo. *J Cell Biol* 199: 1037–1046.
- Stevnsner T, Muftuoglu M, Aamann MD, Bohr VA (2008) The role of Cockayne Syndrome group B (CSB) protein in base excision repair and aging. *Mech Ageing Dev* 129: 441–448.
- Klungland A, Hoss M, Gunz D, Constantinou A, Clarkson SG, et al. (1999) Base excision repair of oxidative DNA damage activated by XPG protein. *Mol Cell* 3: 33–42.
- Bessho T (1999) Nucleotide excision repair 3' endonuclease XPG stimulates the activity of base excision repair enzyme thymine glycol DNA glycosylase. *Nucleic Acids Res* 27: 979–983.
- Oyama M, Wakasugi M, Hama T, Hashidume H, Iwakami Y, et al. (2004) Human NTH1 physically interacts with p53 and proliferating cell nuclear antigen. *Biochem Biophys Res Commun* 321: 183–191.
- Sarker AH, Tsutakawa SE, Kostek S, Ng C, Shin DS, et al. (2005) Recognition of RNA polymerase II and transcription bubbles by XPG, CSB, and TFIIH: insights for transcription-coupled repair and Cockayne Syndrome. *Mol Cell* 20: 187–198.
- Banerjee D, Mandal SM, Das A, Hegde ML, Das S, et al. (2011) Preferential repair of oxidized base damage in the transcribed genes of mammalian cells. *J Biol Chem* 286: 6006–6016.
- Reis AM, Mills WK, Ramachandran I, Friedberg EC, Thompson D, et al. (2012) Targeted detection of in vivo endogenous DNA base damage reveals preferential base excision repair in the transcribed strand. *Nucleic Acids Res* 40: 206–219.
- Guo J, Hanawalt PC, Spivak G (2013) Comet-FISH with strand-specific probes reveals transcription-coupled repair of 8-oxoGuanine in human cells. *Nucleic Acids Res* 41: 7700–7712.
- Marteijn JA, Lans H, Vermeulen W, Hoeijmakers JH (2014) Understanding nucleotide excision repair and its roles in cancer and ageing. *Nat Rev Mol Cell Biol* 15: 465–481.
- DiGiovanna JJ, Kraemer KH (2012) Shining a light on xeroderma pigmentosum. *J Invest Dermatol* 132: 785–796.
- Stefanini M, Botta E, Lanzafame M, Orioli D (2010) Trichothiodystrophy: from basic mechanisms to clinical implications. *DNA Repair (Amst)* 9: 2–10.
- Laugel V, Dalloz C, Durand M, Sauvaud F, Kristensen U, et al. (2010) Mutation update for the CSB/ERCC6 and CSA/ERCC8 genes involved in Cockayne syndrome. *Hum Mutat* 31: 113–126.
- Kraemer KH, Patronas NJ, Schiffmann R, Brooks BP, Tamura D, et al. (2007) Xeroderma pigmentosum, trichothiodystrophy and Cockayne syndrome: a complex genotype-phenotype relationship. *Neuroscience* 145: 1388–1396.
- Antinen A, Nikoskelainen E, Portin R, Kurki T, Erkinjuntti M, et al. (2008) Neurological symptoms and natural course of xeroderma pigmentosum. *Brain* 131: 1979–1989.
- Nakazawa Y, Sasaki K, Mitsutake N, Matsuse M, Shimada M, et al. (2012) Mutations in UVSSA cause UV-sensitive syndrome and impair RNA polymerase II processing in transcription-coupled nucleotide-excision repair. *Nat Genet* 44: 586–592.
- Schwertman P, Lagarou A, Dekkers DH, Raams A, van der Hoek AC, et al. (2012) UV-sensitive syndrome protein UVSSA recruits USP7 to regulate transcription-coupled repair. *Nat Genet* 44: 598–602.
- Zhang X, Horibata K, Saijo M, Ishigami C, Ukai A, et al. (2012) Mutations in UVSSA cause UV-sensitive syndrome and destabilize ERCC6 in transcription-coupled DNA repair. *Nat Genet* 44: 593–597.
- Fei J, Chen J (2012) KIAA1530 is recruited by cockayne syndrome complementation group protein A (CSA) to participate in transcription-coupled repair (TCR). *J Biol Chem* 287: 35118–35126.
- Natale V (2011) A comprehensive description of the severity groups in Cockayne syndrome. *Am J Med Genet A* 155A: 1081–1095.
- Brooks PJ (2013) Blinded by the UV light: how the focus on transcription-coupled NER has distracted from understanding the mechanisms of Cockayne syndrome neurologic disease. *DNA Repair (Amst)* 12: 656–671.
- Cho I, Tsai PF, Lake RJ, Basheer A, Fan HY (2013) ATP-dependent chromatin remodeling by Cockayne syndrome protein B and NAP1-like histone chaperones is required for efficient transcription-coupled DNA repair. *PLoS* 9: e1003407.
- Gregg SQ, Robinson AR, Niedernhofer LJ (2011) Physiological consequences of defects in ERCC1-XPF DNA repair endonuclease. *DNA Repair (Amst)* 10: 781–791.
- Jaspers NG, Raams A, Silengo MC, Wijgers N, Niedernhofer LJ, et al. (2007) First reported patient with human ERCC1 deficiency has cerebro-oculo-facio-skeletal syndrome with a mild defect in nucleotide excision repair and severe developmental failure. *Am J Hum Genet* 80: 457–466.
- Kashiyama K, Nakazawa Y, Pilz DT, Guo C, Shimada M, et al. (2013) Malfunction of nuclease ERCC1-XPF results in diverse clinical manifestations and causes Cockayne syndrome, xeroderma pigmentosum, and Fanconi anemia. *Am J Hum Genet* 92: 807–819.
- Niedernhofer LJ, Garinis GA, Raams A, Lalai AS, Robinson AR, et al. (2006) A new progeroid syndrome reveals that genotoxic stress suppresses the somatotroph axis. *Nature* 444: 1038–1043.
- Lehmann J, Schubert S, Schafer A, Apel A, Laspe P, et al. (2014) An unusual mutation in the XPG gene leads to an internal in-frame deletion and a XP/CS complex phenotype. *Br J Dermatol*. E-pub ahead of print. doi:10.1111/bjd.13035
- Scharer OD (2008) Hot topics in DNA repair: the molecular basis for different disease states caused by mutations in TFIIH and XPG. *DNA Repair (Amst)* 7: 339–344.
- Schafer A, Schubert S, Gratchev A, Seebode C, Apel A, et al. (2013) Characterization of three XPG-defective patients identifies three missense mutations that impair repair and transcription. *J Invest Dermatol* 133: 1841–1849.
- Soltys DT, Rocha CR, Lerner LK, de Souza TA, Munford V, et al. (2013) Novel XPG (ERCC5) mutations affect DNA repair and cell survival after ultraviolet but not oxidative stress. *Hum Mutat* 34: 481–489.
- Nouspikel T, Lalle P, Leadon SA, Cooper PK, Clarkson SG (1997) A common mutational pattern in Cockayne syndrome patients from xeroderma pigmentosum group G: implications for a second XPG function. *Proc Natl Acad Sci U S A* 94: 3116–3121.

57. Emmert S, Slor H, Busch DB, Batko S, Albert RB, et al. (2002) Relationship of neurologic degeneration to genotype in three xeroderma pigmentosum group G patients. *J Invest Dermatol* 118: 972–982.
58. Schafer A, Gratchev A, Seebode C, Hofmann L, Schubert S, et al. (2013) Functional and molecular genetic analyses of nine newly identified XPD-deficient patients reveal a novel mutation resulting in TTD as well as in XP/CS complex phenotypes. *Exp Dermatol* 22: 486–489.
59. Friedberg EC, Meira LB (2006) Database of mouse strains carrying targeted mutations in genes affecting biological responses to DNA damage Version 7. *DNA Repair (Amst)* 5: 189–209.
60. Wijnhoven SW, Hoogervorst EM, de Waard H, van der Horst GT, van Steeg H (2007) Tissue specific mutagenic and carcinogenic responses in NER defective mouse models. *Mutat Res* 614: 77–94.
61. Niedernhofer LJ (2008) Nucleotide excision repair deficient mouse models and neurological disease. *DNA Repair (Amst)* 7: 1180–1189.
62. Jaarsma D, van der Pluijm I, van der Horst GT, Hoeijmakers JH (2013) Cockayne syndrome pathogenesis: Lessons from mouse models. *Mech Ageing Dev* 134: 180–195.
63. Harada YN, Shiomi N, Koike M, Ikawa M, Okabe M, et al. (1999) Postnatal growth failure, short life span, and early onset of cellular senescence and subsequent immortalization in mice lacking the xeroderma pigmentosum group G gene. *Mol Cell Biol* 19: 2366–2372.
64. Tian M, Jones DA, Smith M, Shinkura R, Alt FW (2004) Deficiency in the Nuclease Activity of Xeroderma Pigmentosum G in Mice Leads to Hypersensitivity to UV Irradiation. *Mol Cell Biol* 24: 2237–2242.
65. Shiomi N, Kito S, Oyama M, Matsunaga T, Harada YN, et al. (2004) Identification of the XPG Region That Causes the Onset of Cockayne Syndrome by Using Xpg Mutant Mice Generated by the cDNA-Mediated Knock-In Method. *Mol Cell Biol* 24: 3712–3719.
66. Shiomi N, Mori M, Kito S, Harada YN, Tanaka K, et al. (2005) Severe growth retardation and short life span of double-mutant mice lacking Xpa and exon 15 of Xpg. *DNA Repair (Amst)* 4: 351–357.
67. Laposo RR, Huang EJ, Cleaver JE (2007) Increased apoptosis, p53 up-regulation, and cerebellar neuronal degeneration in repair-deficient Cockayne syndrome mice. *Proc Natl Acad Sci U S A* 104: 1389–1394.
68. van der Pluijm I, Garinis GA, Brandt RM, Gorgels TG, Wijnhoven SW, et al. (2007) Impaired genome maintenance suppresses the growth hormone–insulin-like growth factor 1 axis in mice with Cockayne syndrome. *PLoS Biol* 5: e2.
69. Murai M, Enokido Y, Inamura N, Yoshino M, Nakatsu Y, et al. (2001) Early postnatal ataxia and abnormal cerebellar development in mice lacking Xeroderma pigmentosum Group A and Cockayne syndrome Group B DNA repair genes. *Proc Natl Acad Sci U S A* 98: 13379–13384.
70. Andressoo JO, Weeda G, de Wit J, Mitchell JR, Beems RB, et al. (2009) An Xpb mouse model for combined xeroderma pigmentosum and cockayne syndrome reveals progeroid features upon further attenuation of DNA repair. *Mol Cell Biol* 29: 1276–1290.
71. Andressoo JO, Mitchell JR, de Wit J, Hoogstraten D, Volker M, et al. (2006) An Xpd mouse model for the combined xeroderma pigmentosum/Cockayne syndrome exhibiting both cancer predisposition and segmental progeria. *Cancer Cell* 10: 121–132.
72. Weeda G, Donker I, de Wit J, Morreau H, Janssens R, et al. (1997) Disruption of mouse ERCC1 results in a novel repair syndrome with growth failure, nuclear abnormalities and senescence. *Curr Biol* 7: 427–439.
73. Sakai K, Miyazaki J (1997) A transgenic mouse line that retains Cre recombinase activity in mature oocytes irrespective of the cre transgene transmission. *Biochem Biophys Res Commun* 237: 318–324.
74. Nakane H, Takeuchi S, Yuba S, Saijo M, Nakatsu Y, et al. (1995) High incidence of ultraviolet-B or chemical-carcinogen-induced skin tumours in mice lacking the xeroderma pigmentosum group A gene. *Nature* 377: 165–168.
75. Jaspers NG, Raams A, Kelner MJ, Ng JM, Yamashita YM, et al. (2002) Antitumour compounds illudin S and Irofulven induce DNA lesions ignored by global repair and exclusively processed by transcription- and replication-coupled repair pathways. *DNA Repair (Amst)* 1: 1027–1038.
76. Vo N, Seo HY, Robinson A, Sowa G, Bentley D, et al. (2010) Accelerated aging of intervertebral discs in a mouse model of progeria. *J Orthop Res* 28: 1600–1607.
77. de Boer J, Andressoo JO, de Wit J, Huijman J, Beems RB, et al. (2002) Premature aging in mice deficient in DNA repair and transcription. *Science* 296: 1276–1279.
78. Nicolajje C, Diderich KE, Botter SM, Priemel M, Waarsing JH, et al. (2012) Age-related skeletal dynamics and decrease in bone strength in DNA repair deficient male trichothiodystrophy mice. *PLoS ONE* 7: e35246.
79. Diderich KE, Nicolajje C, Priemel M, Waarsing JH, Day JS, et al. (2012) Bone fragility and decline in stem cells in prematurely aging DNA repair deficient trichothiodystrophy mice. *Age (Dordr)* 34: 845–861.
80. Tian M, Shinkura R, Shinkura N, Alt FW (2004) Growth Retardation, Early Death, and DNA Repair Defects in Mice Deficient for the Nucleotide Excision Repair Enzyme XPF. *Mol Cell Biol* 24: 1200–1205.
81. McWhir J, Selfridge J, Harrison DJ, Squires S, Melton DW (1993) Mice with DNA repair gene (ERCC-1) deficiency have elevated levels of p53, liver nuclear abnormalities and die before weaning. *Nat Genet* 5: 217–224.
82. Gregg SQ, Gutierrez V, Robinson AR, Woodell T, Nakao A, et al. (2012) A mouse model of accelerated liver aging caused by a defect in DNA repair. *Hepatology* 55: 609–621.
83. Selfridge J, Hsia KT, Redhead NJ, Melton DW (2001) Correction of liver dysfunction in DNA repair-deficient mice with an ERCC1 transgene. *Nucleic Acids Res* 29: 4541–4550.
84. Garinis GA, Uittenboogaard LM, Stachelscheid H, Fouteri M, van Ijcken W, et al. (2009) Persistent transcription-blocking DNA lesions trigger somatic growth attenuation associated with longevity. *Nat Cell Biol* 11: 604–615.
85. van de Ven M, Andressoo JO, Holcomb VB, von Lindern M, Jong WM, et al. (2006) Adaptive stress response in segmental progeria resembles long-lived dwarfism and calorie restriction in mice. *PLoS Genet* 2: e192.
86. Kensler TW, Wakabayashi N, Biswal S (2007) Cell survival responses to environmental stresses via the Keap1-Nrf2-ARE pathway. *Annu Rev Pharmacol Toxicol* 47: 89–116.
87. el-Deiry WS (1998) Regulation of p53 downstream genes. *Semin Cancer Biol* 8: 345–357.
88. Chiphchase MD, O'Neill M, Melton DW (2003) Characterization of premature liver polyploidy in DNA repair (Ercc1)-deficient mice. *Hepatology* 38: 958–966.
89. Borgesius NZ, de Waard MC, van der Pluijm I, Omrani A, Zondag GC, et al. (2011) Accelerated age-related cognitive decline and neurodegeneration, caused by deficient DNA repair. *J Neurosci* 31: 12543–12553.
90. de Waard MC, van der Pluijm I, Zuiderveen Borgesius N, Comley LH, Haasdijk ED, et al. (2010) Age-related motor neuron degeneration in DNA repair-deficient Ercc1 mice. *Acta Neuropathol* 120: 461–475.
91. Jaarsma D, van der Pluijm I, de Waard MC, Haasdijk ED, Brandt R, et al. (2011) Age-related neuronal degeneration: complementary roles of nucleotide excision repair and transcription-coupled repair in preventing neuropathology. *PLoS Genet* 7: e1002405.
92. de Graaf EL, Vermeij WP, de Waard MC, Rijksen Y, van der Pluijm I, et al. (2013) Spatio-temporal analysis of molecular determinants of neuronal degeneration in the aging mouse cerebellum. *Mol Cell Proteomics* 12: 1350–1362.
93. Adalbert R, Coleman MP (2013) Review: Axon pathology in age-related neurodegenerative disorders. *Neuropathol Appl Neurobiol* 39: 90–108.
94. Weidenheim KM, Dickson DW, Rapin I (2009) Neuropathology of Cockayne syndrome: Evidence for impaired development, premature aging, and neurodegeneration. *Mech Ageing Dev* 130: 619–636.
95. Postic C, Shiota M, Niswender KD, Jetton TL, Chen Y, et al. (1999) Dual roles for glucokinase in glucose homeostasis as determined by liver and pancreatic beta cell-specific gene knock-outs using Cre recombinase. *J Biol Chem* 274: 305–315.
96. Beyer TA XW, Teupser D, auf dem Keller U, Bugnon P, Hildt E, et al. (2008) Impaired liver regeneration in Nrf2 knockout mice: role of ROS-mediated insulin/IGF-1 resistance. *EMBO J* 9: 212–223.
97. Itoh M, Hayashi M, Shioda K, Minagawa M, Isa F, et al. (1999) Neurodegeneration in hereditary nucleotide repair disorders. *Brain Dev* 21: 326–333.
98. Koob M, Laugel V, Durand M, Fothergill H, Daloz C, et al. (2010) Neuroimaging in Cockayne syndrome. *AJNR Am J Neuroradiol* 31: 1623–1630.
99. Hayashi M, Miwa-Saito N, Tanuma N, Kubota M (2012) Brain vascular changes in Cockayne syndrome. *Neuropathology* 32: 113–117.
100. Iwasato T, Nomura R, Ando R, Ikeda T, Tanaka M, et al. (2004) Dorsal telencephalon-specific expression of Cre recombinase in PAC transgenic mice. *Genesis* 38: 130–138.
101. Lemon RN, Johansson RS, Westling G (1995) Corticospinal control during reach, grasp, and precision lift in man. *J Neurosci* 15: 6145–6156.
102. Rotshenker S (2009) The role of Galectin-3/MAC-2 in the activation of the innate-immune function of phagocytosis in microglia in injury and disease. *J Mol Neurosci* 39: 99–103.
103. Lee SK, Yu SL, Prakash L, Prakash S (2002) Requirement of yeast RAD2, a homolog of human XPG gene, for efficient RNA polymerase II transcription. implications for Cockayne syndrome. *Cell* 109: 823–834.
104. Thorel F, Constantinou A, Dunand-Sauthier I, Nospikel T, Lalle P, et al. (2004) Definition of a short region of XPG necessary for TFIIH interaction and stable recruitment to sites of UV damage. *Mol Cell Biol* 24: 10670–10680.
105. Trego KS, Chernikova SB, Davalos AR, Perry JJ, Finger LD, et al. (2011) The DNA repair endonuclease XPG interacts directly and functionally with the WRN helicase defective in Werner syndrome. *Cell Cycle* 10: 1998–2007.
106. Brace LE, Vose SC, Vargas DF, Zhao S, Wang XP, et al. (2013) Lifespan extension by dietary intervention in a mouse model of Cockayne syndrome uncouples early postnatal development from segmental progeria. *Ageing Cell* 12: 1144–1147.
107. Andressoo JO, Jans J, de Wit J, Coin F, Hoogstraten D, et al. (2006) Rescue of progeria in trichothiodystrophy by homozygous lethal Xpd alleles. *PLoS Biol* 4: e322.
108. Vermeulen W, Jaeken J, Jaspers NG, Bootsma D, Hoeijmakers JH (1993) Xeroderma pigmentosum complementation group G associated with Cockayne syndrome. *Am J Hum Genet* 53: 185–192.
109. Schumacher B, van der Pluijm I, Moorhouse MJ, Kosteus T, Robinson AR, et al. (2008) Delayed and accelerated aging share common longevity assurance mechanisms. *PLoS Genet* 4: e1000161.
110. Vermeij WP, Hoeijmakers JHJ, Pothof J (2014) Aging: Not All DNA Damage is Equal. *Curr Opin Genet Dev* In press.

111. Sun XZ, Harada YN, Takahashi S, Shiomi N, Shiomi T (2001) Purkinje cell degeneration in mice lacking the xeroderma pigmentosum group G gene. *J Neurosci Res* 64: 348–354.
112. Vegh MJ, de Waard MC, van der Pluijm I, Ridwan Y, Sassen MJ, et al. (2012) Synaptic proteome changes in a DNA repair deficient *erc1* mouse model of accelerated aging. *J Proteome Res* 11: 1855–1867.
113. Melis JP, Wijnhoven SW, Beems RB, Roodbergen M, van den Berg J, et al. (2008) Mouse models for xeroderma pigmentosum group A and group C show divergent cancer phenotypes. *Cancer Res* 68: 1347–1353.
114. Lee YJ, Park SJ, Ciccone SL, Kim CR, Lee SH (2006) An in vivo analysis of MMC-induced DNA damage and its repair. *Carcinogenesis* 27: 446–453.
115. D'Errico M, Parlanti E, Teson M, Degan P, Lemma T, et al. (2007) The role of CSA in the response to oxidative DNA damage in human cells. *Oncogene* 26: 4336–4343.
116. Spivak G, Hanawalt PC (2006) Host cell reactivation of plasmids containing oxidative DNA lesions is defective in Cockayne syndrome but normal in UV-sensitive syndrome fibroblasts. *DNA Repair (Amst)* 5: 13–22.
117. de Waard H, de Wit J, Gorgels TG, van den Aardweg G, Andressoo JO, et al. (2003) Cell type-specific hypersensitivity to oxidative damage in CSB and XPA mice. *DNA Repair (Amst)* 2: 13–25.
118. de Waard H, de Wit J, Andressoo JO, van Oostrom CT, Riis B, et al. (2004) Different effects of CSA and CSB deficiency on sensitivity to oxidative DNA damage. *Mol Cell Biol* 24: 7941–7948.
119. Halliwell B (2003) Oxidative stress in cell culture: an under-appreciated problem? *FEBS Letters* 540: 3–6.
120. Totonchy MB, Tamura D, Pantell MS, Zalewski C, Bradford PT, et al. (2013) Auditory analysis of xeroderma pigmentosum 1971–2012: hearing function, sun sensitivity and DNA repair predict neurological degeneration. *Brain* 136: 194–208.
121. Schaft J, Ashery-Padan R, van der Hoeven F, Gruss P, Stewart AF (2001) Efficient FLP recombination in mouse ES cells and oocytes. *Genesis* 31: 6–10.
122. Waarsing JH, Day JS, Weinans H (2004) An improved segmentation method for in vivo microCT imaging. *J Bone Miner Res* 19: 1640–1650.
123. Botter SM, Glasson SS, Hopkins B, Clockaerts S, Weinans H, et al. (2009) ADAMTS5^{-/-} mice have less subchondral bone changes after induction of osteoarthritis through surgical instability: implications for a link between cartilage and subchondral bone changes. *Osteoarthritis Cartilage* 17: 636–645.
124. Pfaffl MW (2001) A new mathematical model for relative quantification in real-time RT-PCR. *Nucleic Acids Res* 29: e45.